Nano Research

Open Access

Research Article

Poly(L-lactic-co-caprolactone)-nano hydroxyapatite promotes periodontal bone regeneration via mitochondrial metabolism-driven macrophage reprogramming

Pei Cao[1,§], Nan Li[2,§], Yuan-qing Liu[1], Yong Zhang[3], Pei-hui Zou[4], Jin Wu[5], Yu Cai[1], Chen-hao Yu[1], Liang Chen[1], Qing-xian Luan[1]✉, and Jia Liu[1]✉

[1] *Department of Periodontology, Peking University School and Hospital of Stomatology & National Center of Stomatology & National Clinical Research Center for Oral Diseases & National Engineering Laboratory for Digital and Material Technology of Stomatology & Beijing Key Laboratory of Digital Stomatology, Beijing 100081, China*

[2] *Department of Stomatology, Shenzhen People's Hospital (The First Affiliated Hospital of Southern University of Science and Technology; Second Clinical Medical School of Jinan University), Shenzhen 518020, China*

[3] *First Clinical Division, Peking University School and Hospital of Stomatology & National Center of Stomatology & National Clinical Research Center for Oral Diseases & National Engineering Laboratory for Digital and Material Technology of Stomatology & Beijing Key Laboratory of Digital Stomatology, Beijing 100081, China*

[4] *Seventh Clinical Division, Peking University School and Hospital of Stomatology & National Center of Stomatology & National Clinical Research Center for Oral Diseases & National Engineering Laboratory for Digital and Material Technology of Stomatology & Beijing Key Laboratory of Digital Stomatology, Beijing 100081, China*

[5] *Department of Orthopaedics, the 909S1 Hospital, School of Medicine, Xiamen University, Zhangzhou 363000, China*

§ *Pei Cao and Nan Li contributed equally to this work.*

Cite this article: *Nano Research*, **2026**, *19*, 94908577. https://doi.org/10.26599/NR.2026.94908577

ABSTRACT: Periodontitis, a chronic inflammatory disease causing progressive bone loss, demands biomaterials that simultaneously resolve inflammation and promote regeneration. Poly(L-lactic-co-caprolactone)-nano hydroxyapatite (PLCL-nHA) combines mechanical durability with bioactive potential, yet its precise immunomodulatory actions within inflammatory microenvironments remain unclear. This study demonstrates that PLCL-nHA restores periodontal homeostasis by suppressing inflammatory cascades and steering macrophage functional reprogramming. In a murine periodontitis model, PLCL-nHA implantation reduced alveolar bone resorption, altered the gingival microbiota profile (including reduction of Lactobacillus/Enterococcus), and suppressed osteoclastic activity. *In vitro*, PLCL-nHA suppressed LPS-induced pro-inflammatory cytokines and oxidative stress while promoting M2 macrophage polarization. Mechanistically, PLCL-nHA enhanced mitochondrial energy metabolism, which inhibited nuclear factor kappa B (NF-κB) activation. Rat bone defects confirmed accelerated inflammatory resolution and osteogenesis. These findings establish PLCL-nHA as a dual-functional scaffold that coordinates immunometabolic adaptation and tissue repair, providing a paradigm for metabolism-oriented resolution of inflammation in periodontitis and related osteolytic disorders.

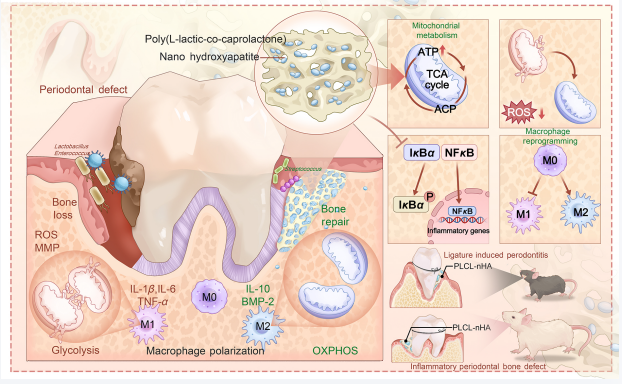

KEYWORDS: poly(L-lactic-co-caprolactone)-nanohydroxyapatite (PLCL-nHA) composite, periodontal bone regeneration, macrophage polarization, metabolic reprogramming, nuclear factor kappa B (NF-κB) signaling pathway

1 Introduction

Periodontitis is one of the most prevalent chronic inflammatory diseases worldwide, leading to progressive destruction of periodontal ligament and alveolar bone [1, 2]. While microbial dysbiosis initiates periodontitis [3], the persistence of

Received: January 3, 2026; **Revised:** February 10, 2026
Accepted: February 13, 2026

✉Address correspondence to Qing-xian Luan, kqluanqx@126.com; Jia Liu, dentistliujia@126.com

inflammation—fueled by dysregulated immune responses and oxidative stress—is now recognized as the primary driver of tissue catabolism and failed regeneration [4]. Pro-inflammatory cytokines (e.g., tumor necrosis factor-α (TNF-α), interleukin-1 beta (IL-1β)) suppress osteoblast differentiation and promote osteoclast activation [5, 6], while matrix metalloproteinases (MMPs) degrade the extracellular matrix, disrupting the regenerative scaffold structure [7]. Current protocols emphasize pre-operative inflammation control (e.g., scaling, anti-inflammatory drugs) to reduce bacterial load and acute inflammation [8]; however, intraoperative limitations persist: even after debridement of inflamed tissues, conventional bone grafts lack inherent anti-inflammatory activity, leaving residual chronic inflammation unaddressed during the healing phase.

Classic and widely used periodontal regeneration techniques, such as Guided Tissue Regeneration (GTR) combined with bone grafting, still rely on bone substitute materials to provide physical scaffolding and osteoconductivity. Although autologous bone grafts remain the "gold standard", their clinical application is limited by donor site complications and insufficient bone volume [9]. Traditional bone substitutes (e.g., deproteinized bovine bone Bio-Oss® and β-tricalcium phosphate) exhibit excellent osteoconductivity but fail to actively regulate immune responses. Additionally, particulate bone powders are difficult to mold and stabilize during surgery, often leading to displacement or collapse [10].

Recent studies highlight that mitochondrial dysfunction and oxidative stress in the periodontal inflammatory microenvironment are critical barriers to bone regeneration [11]. Excessive reactive oxygen species (ROS) not only impair osteoblast differentiation [5, 12], but also exacerbate local inflammation by activating the NF-κB pathway [6, 13]. To address these issues, researchers have developed materials with antioxidant and immunomodulatory functions by loading exogenous bioactive molecules (e.g., cytokines, exosomes) or incorporating functional groups [14]. For example, Gao et al. designed a xylitol-succinic acid composite hydrogel that inhibits Toll-like receptor 4 (TLR4)/myeloid differentiation factor 2 (MyD2) signaling and downregulates the NF-κB pathway to suppress inflammation [13]. Yu et al. developed an injectable hydrogel composed of gelatin and lysine copolymers, which scavenges ROS, mitigates inflammation, and promotes periodontal repair [15]. Deng et al. incorporated mesenchymal stem cell-derived exosomes into a hydrogel delivery system to regulate macrophage polarization toward the M2 phenotype, enhancing periodontal regeneration [16]. Wang et al. utilized a hydrogel system loaded with natural compound cordycepin and microspheres to alleviate inflammation via the Nrf2 pathway [17]. Additionally, Gong et al. fabricated a metformin-loaded polydopamine-gelatin patch that reduces oxidative stress, inhibits M1 macrophage polarization, and improves the periodontal microenvironment [11]. However, these strategies face inherent limitations: (1) their functionality depends on exogenous molecules, posing risks of molecular instability, uncontrolled release kinetics, and potential immunogenicity; (2) the complex integration of multiple functional modules increases manufacturing difficulty, hindering clinical translation; and (3) drug-loaded hydrogels often exhibit suboptimal mechanical properties and degradation rates compared to conventional bone graft materials [18].

Poly(L-lactic-co-caprolactone) (PLCL), a copolymer synthesized from L-lactide and ε-caprolactone, demonstrates excellent biocompatibility. Its degradation products are naturally metabolized *in vivo* [19], and lactate—a glycolysis metabolite—has been shown to regulate immune responses [20, 21]. Nano-hydroxyapatite (nHA), another immunomodulatory nanoparticle, interacts with immune cells through its unique surface properties and bioactivity, influencing inflammatory responses and bone metabolism [22]. Specifically, nHA can promote M2 macrophage polarization, thereby suppressing inflammation and facilitating tissue repair [22, 23]. Although PLCL-nHA composites have been extensively studied for bone defect repair [24–26], their potential in periodontal regeneration and their ability to regulate the complex immune microenvironment remain poorly explored.

Herein, this study aims to investigate the potential of PLCL-nHA in promoting periodontal bone regeneration, focusing on its ability to modulate macrophage-mediated inflammation and enhance bone formation. Using *in vitro* and *in vivo* models, we explore the mechanisms underlying their anti-inflammatory and osteogenic effects, including their impact on macrophage metabolism, mitochondrial function, and local microbiota modulation. By addressing the critical challenges in periodontal regeneration, this research seeks to provide a new material-based strategy for improving clinical outcomes in periodontitis treatment and contribute to the development of advanced biomaterials for periodontal tissue regeneration.

2 Results and discussion

2.1 PLCL-nHA exhibits optimized physicochemical, mechanical properties, and biocompatibility

The as-prepared material macroscopically exhibits a moderately firm, dough-like consistency with excellent moldability (Fig. 1(a)). Its water contact angle was measured to be 86.72°, indicating moderate hydrophilicity (Fig. 1(b)). Compared with reported values for PLCL [27], this reduced contact angle may support protein adsorption [28] while being more conducive to early cell–material interactions in the periodontal microenvironment [29]. The X-ray diffraction (XRD) pattern of HAP (Fig. 1(c)) was consistent with the standard peaks (PDF card No. 74-0565). Fourier-transform infrared spectroscopy (FTIR) confirmed the successful incorporation of nHA into the PLCL matrix, as evidenced by characteristic phosphate and carbonate peaks (Fig. 1(e)). Scanning electron microscopy (SEM) revealed that PCL-nHA exhibited a uniform nano-scale particle distribution with a diameter of approximately 50 nm. While rare 10 μm-scale pores are observed, their sparse distribution means that the majority of the surface remains low-roughness (Fig. 1(d)). To enable material-derived biological activity, the scaffold was immersed in simulated body fluid for 4 weeks. Surface degradation and pore formation promoted the release of nanoscale components, with nanoparticle tracking analysis confirming 100 nm particles consistent with the designed nHA (Figs. 1(d) and 1(f)). XRD patterns and FTIR spectra of residual material confirmed chemical stability of nHA phase (Figs. 1(c) and 1(e)). The force-deformation curve (Fig. 1(g)) showed a compressive strength of 4.07 MPa and an elastic modulus of 24.1 MPa, suitable for surgical handling. Post-degradation testing under physiological conditions (37 °C, 100% humidity) demonstrated retained mechanical properties (1.78 MPa strength, 14.5 MPa modulus), providing sufficient structural support during early bone regeneration phase [30]. Furthermore, the pH variation

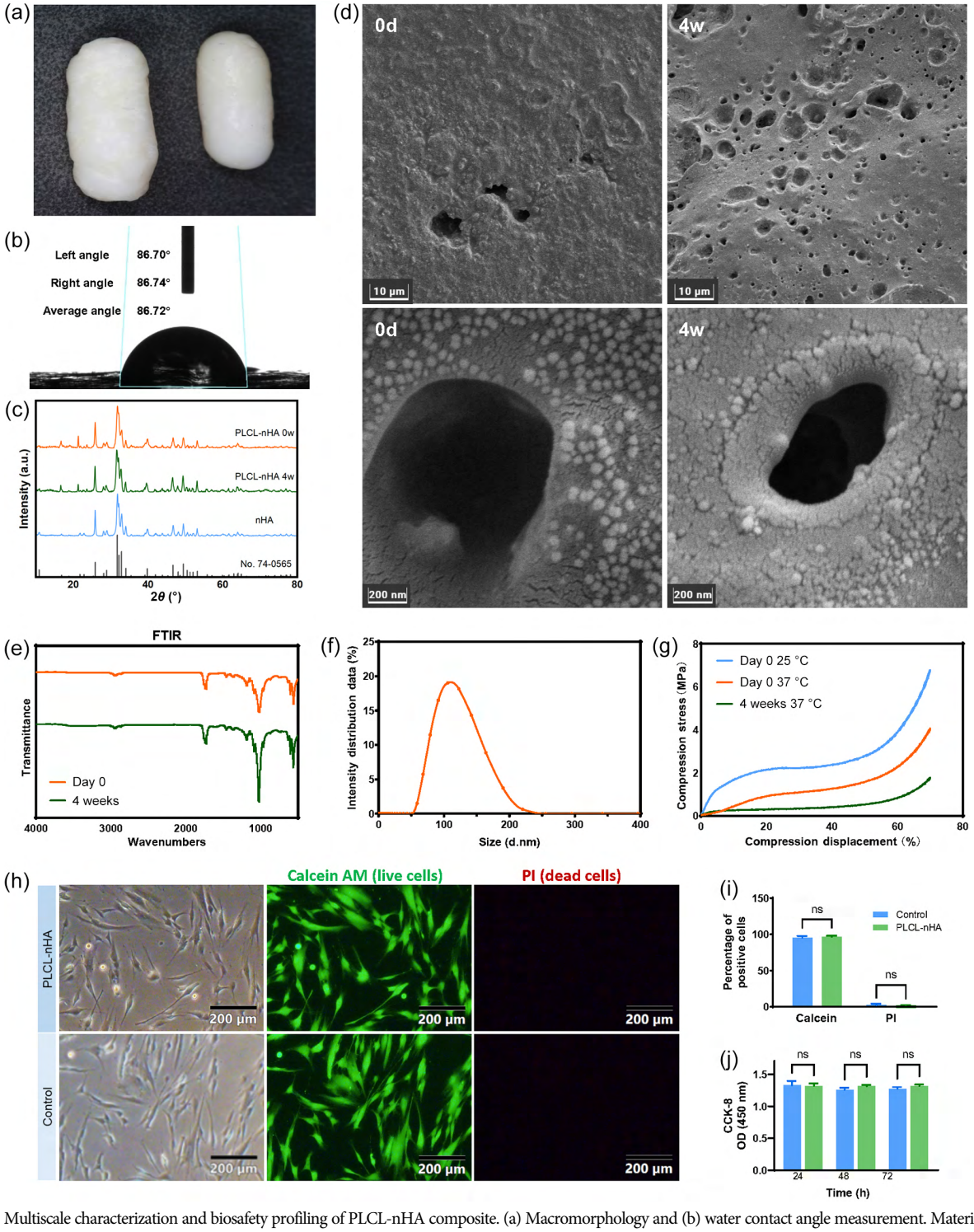

Figure 1 Multiscale characterization and biosafety profiling of PLCL-nHA composite. (a) Macromorphology and (b) water contact angle measurement. Material stability analysis: (c) XRD and (e) FTIR analyses before and after SBF immersion; (d) SEM micrographs showing pre-/post-SBF (37 °C, 4 weeks) surface nanostructure (scale bars: 10 μm (2k×), 200 nm (100k×)). (f) Nanoparticle size distribution in PLCL-nHA composite extract. (g) Stress–strain curves under three conditions: baseline (25 °C), baseline (37 °C), and post-SBF immersion (37 °C). Cytocompatibility validation: (h) Live/dead staining of hPDLCs after 24-h treatment; (i) flow cytometry quantification of viable/apoptotic cell ratios; (j) CCK-8 absorbance values of hPDLCs treated with PLCL-nHA extract for 24, 48, and 72 h. Data presented as mean ± standard error of the mean (s.e.m.) ($n = 3$); $^{***}P < 0.001$, $^{**}P < 0.01$, $^{*}P < 0.05$, ns: not significant (one-way ANOVA).

of the degradation medium was monitored. Although the degradation of PLCL led to a mild pH decrease over time, the incorporation of nano-hydroxyapatite (nHA) effectively mitigated excessive acidification (Fig. S1 in the Electronic Supplementary Material (ESM)), maintaining the pH of the PLCL-nHA system within a near-physiological range [31]. This stabilized microenvironment is favorable for bone regeneration, as excessive acidification has been reported to exacerbate inflammatory responses and enhance osteoclastic activity [32].

Biocompatibility evaluation showed similar cell viability by cell

counting kit-8 (CCK-8) and percentage of live (green) cells in human periodontal ligament cells (hPDLCs) cultured in PLCL-nHA compared to the control group (Fig. 1(j)), with live/dead staining indicating > 95% cell viability (Figs. 1(h) and 1(i)), indicating excellent biocompatibility, consistent with previously reported biological properties of PLCL and nHA.

2.2 PLCL-nHA reduces inflammatory bone loss in a periodontitis model.

Periodontitis manifests as an inflammatory response of the gingival sulcular epithelium and connective tissue to microbial plaque, leading to collagen degradation and alveolar bone resorption. The murine ligature-induced periodontitis model, established by placing silk ligatures around the cervical area of teeth to promote plaque accumulation, effectively mimics human periodontal inflammation. Using this model, we investigated whether our material could modulate immune-inflammatory responses and improve the periodontal microenvironment.

16S rRNA sequencing was conducted (Fig. 2(a)). Venn diagram (Fig. 2(b)) and rarefaction curves (Figs. 2(c) and 2(d)) verified group-specific operational taxonomic unit (OTU) distribution and adequate sampling. Further analysis demonstrated an increased α-diversity in ligature groups compared to healthy controls (Fig. 2(e)), as an distinct β-diversity clustering confirming ligature-induced microbial shifts (Fig. 2(f)) [33]. Compared to the control group, the relative abundance of Streptococcus decreased post-ligation (Figs. 2(g)–2(k)), while Lactobacillus and Enterococcus increased (Figs. 2(g)–2(k))—a trend consistent with previous reports [34]. Although PLCL-nHA implantation showed no significant impact on α-diversity (Fig. 2(e)), species composition analysis revealed its partial reversal of dysbiosis by restoring Streptococcus (28.8% ± 6.6% vs. 0.3% ± 0.1% in ligature group) and reducing pathobionts, such as Lactobacillus (1.3% ± 0.5% vs. 15.2% ± 1.5% in ligature group, $P < 0.05$) and Enterococcus (2.6% ± 1.1% vs. 8.0% ± 1.1% in ligature group, $P < 0.05$) (Figs. 2(j1)–2(j3)). Although such a partial restoration of the gingival microbial profile was observed *in vivo*, the present study does not support a direct antibacterial or bacteriostatic effect of the material. *In vitro* assays demonstrated that PLCL-nHA exhibited a relatively smooth surface with reduced bacterial adhesion compared to commercial Bio-Oss, yet no direct inhibition of bacterial growth was observed (Fig. S2 in the ESM). Given the well-established bidirectional interaction between host immune responses and microbial ecology in periodontitis [35], we therefore speculate that the observed microbial shifts are more likely secondary to the attenuation of local inflammation and restoration of periodontal immune homeostasis, rather than a direct material–microbe interaction. Importantly, such inflammation-driven microbial remodeling may still be functionally relevant, as the reduced abundance of specific taxa could limit the local burden of pro-inflammatory microbial metabolites and virulence-associated factors [36], thereby alleviating host immunometabolic stress and creating a microenvironment more permissive for tissue repair.

Subsequently, radiographic and histological evaluations were performed (Fig. 3(a)). Revealed by micro computed tomography (Micro-CT) analysis, Lig + PLCL-nHA group exhibited less bone resorption (0.29 ± 0.01 mm vs. 0.52 ± 0.02 mm, $P < 0.01$), higher bone mineral density (1165 ± 109 hounsfield unit (HU) vs. 526 ± 102 HU, $P < 0.01$) and increased bone volume fraction (bone volume/total volume (BV/TV): 37.0% ± 4.0% vs. 16.3% ± 2.0%, $P < 0.01$), compared to ligature groups (Figs. 3(b), 3(f1)–3(f3)). Histologically, hematoxylin and eosin (H&E) staining demonstrated reduced inflammatory cell infiltration in epithelial tissues, while tartrate-resistant acid phosphatase (TRAP) staining showed fewer osteoclasts in material-treated specimens (Figs. 3(c), 3(d), 3(g1), and 3(g2)). These findings suggest that PLCL-nHA likely exerts its anti-inflammatory and osteoprotective effects, concomitant with beneficial restructuring of the gingival sulcus microbiota composition.

Given macrophages' pivotal role in regenerative immunomodulation [37] and previous reports on nano-hydroxyapatite regulating macrophage polarization [38, 39], we assessed macrophage polarization via immunofluorescence. The PLCL-nHA composite altered the $CD86^+$ (M1)/$CD206^+$ (M2) ratio in gingival connective tissues (Fig. 3(e)). Consistent with these findings, preliminary studies by our collaborators demonstrated that materials with analogous compositions promote M2 polarization of bone marrow-derived macrophage (BMDM)-derived macrophages *in vitro* [25], suggesting that macrophage modulation may represent a key mechanistic underpinning of their therapeutic effects. However, comprehensive *in vitro* validation is required to conclusively establish this immunoregulatory axis.

2.3 PLCL-nHA reduces ROS levels and modulates macrophage-mediated inflammatory responses

To mechanistically validate *in vivo* observations and dissect the responses underpinning the PLCL-nHA's immunometabolic regulation, we conducted a series of *in vitro* investigations using inflammatory model using LPS-stimulated macrophages (Fig. 4(a)) [39].

Following LPS stimulation, macrophages demonstrated upregulation of pro-inflammatory cytokines (TNF-α: 108.8 ± 3.5 pg/mL, IL-6: 203.0 ± 1.7 pg/mL, and IL-1β: 130.9 ± 2.7 pg/mL) (Fig. 4(b)) and 3.1-fold induction of *iNOS* mRNA expression versus untreated controls ($P < 0.001$) (Fig. 4(d)). PLCL-nHA extract treatment significantly attenuated this inflammatory cascade, reducing cytokine secretion (TNF-$\alpha\downarrow$ 37.5%, $P < 0.001$; IL-6$\downarrow$ 44.4%, $P < 0.001$; IL-1$\beta\downarrow$ 42.4%, $P < 0.001$) through enzyme-linked immunosorbent assay (ELISA) quantification, while quantitative polymerase chain reaction (qPCR) revealed parallel reductions in inducible nitric oxide synthase (iNOS) and cytokines (Figs. 4(b) and 4(d)). These inflammatory substances are known to worsen local inflammation, damage periodontal tissues, and block successful tissue regeneration [40], the inhibition of these cytokines *in vitro* demonstrates anti-inflammatory capacity of PLCL-nHA.

Notably, PLCL-nHA also exhibited dual-phase immunomodulation: under basal conditions, it induced upregulation of M2-associated markers (IL-10: 402% ± 43%; arginase 1 (ARG1): 276% ± 40% $P < 0.001$); more crucially, it reversed LPS-mediated suppression of anti-inflammatory genes, restoring IL-10 and ARG1 expression to 245% ± 27% and 130% ± 15% of baseline levels respectively (vs. 31% ± 2% and 24% ± 2% in LPS group) (Fig. 4(c)). Furthermore, immunofluorescence co-staining revealed that PLCL-nHA treatment significantly upregulated CD206 expression while suppressing CD86 signal (Fig. 4(e) and Fig. S3(a) in the ESM), which was confirmed by flow cytometric quantification demonstrating that PLCL-nHA treatment elevated the M2 macrophage population ($CD206^+$ cell proportion 44.9% ± 0.5% vs. 14.3% ± 0.3% in control, $P < 0.001$) (Fig. 4(f)). In inflammatory microenvironment mimicked by LPS challenge, it

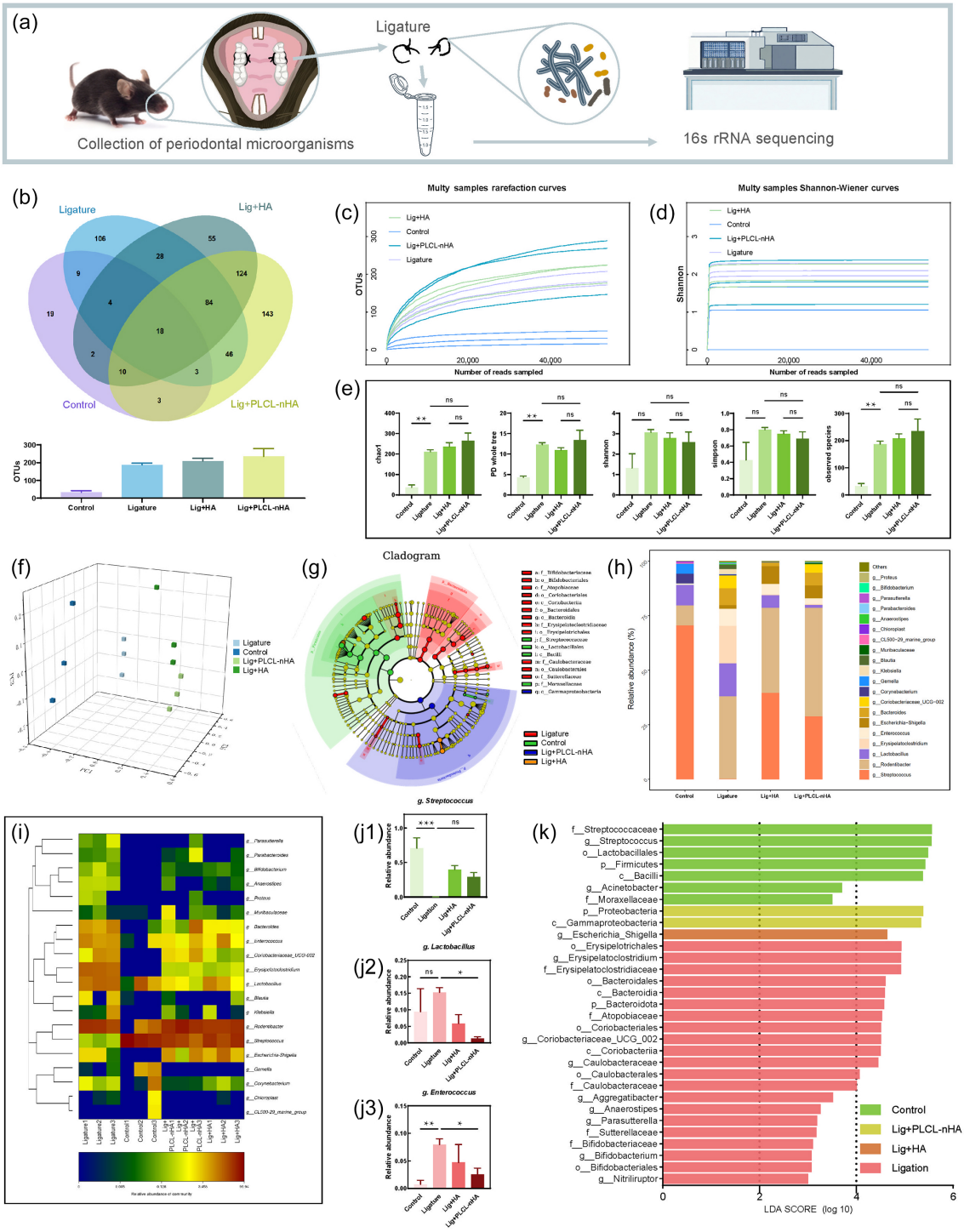

Figure 2 Microbial profiling of gingival sulcus/pocket in murine periodontitis model. (a) Experimental workflow: Schematic of microbial sampling via silk thread collection from gingival sulcus/pocket. (b) Venn diagram and (c) and (d) rarefaction curves confirming group-specific OTU distribution and sampling adequacy (good's coverage > 99.5%). (e) Alpha diversity analysis. (f) Beta diversity: PCoA plot (Bray-Curtis) demonstrating distinct clustering among groups. (g) Heatmap and (h) cladogram illustrating ligation-enriched genera, while (j1)–(j3) PLCL-nHA suppressed pathobionts. (k) LEfSe analysis identified discriminative species (linear discriminant analysis (LDA) score > 3.5). Data: mean ± s.e.m. (n = 3 biological replicates); ***P < 0.001, **P < 0.01, *P < 0.05, ns: not significant (one-way ANOVA with Tukey's test).

effectively suppressed M1 polarization, reducing CD86$^+$ cells from 43.0% ± 3.0% to 22.6% ± 0.6% (P < 0.01), indicating material-driven macrophage polarization towards anti-inflammatory phenotype (Figs. 4(e) and 4(f)).

The enhanced M2 polarization by PLCL-nHA is also critical for resolving inflammation and promoting tissue repair [41]. M2 macrophages are known to secrete anti-inflammatory cytokines, such as IL-10, and play a pivotal role in tissue remodeling [42]. By mitigating excessive inflammatory responses and enhancing M2 polarization, PLCL-nHA helps create a microenvironment conducive to tissue healing and regeneration [43].

Recent studies have highlighted the pivotal role of oxidative

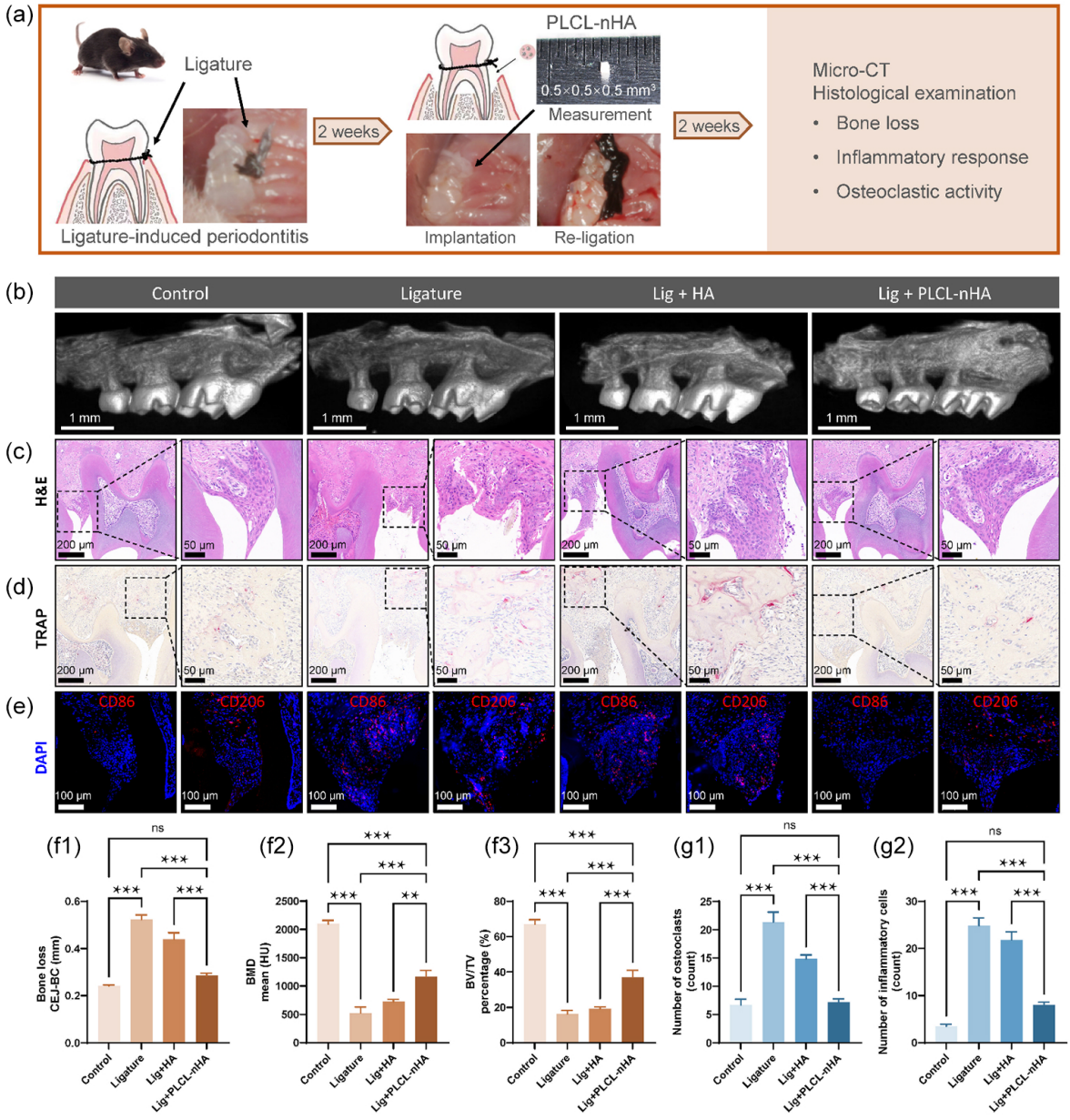

Figure 3 Comprehensive evaluation of periodontal inflammation and immune modulation. (a) Schematic of experimental design and intraoperative photographs: Material implantation protocol and therapeutic timeline in murine periodontitis model. (b) Representative Micro-CT 3D reconstructions: Alveolar bone loss patterns at maxillary second molars. Histological characterization: (c) H&E staining showing epithelial hyperplasia and inflammatory infiltrates; (d) TRAP staining demonstrating osteoclast distribution along bone surfaces. (e) Macrophage polarization: Immunofluorescence co-staining of $CD86^+$ (M1, red) or $CD206^+$ (M2, red) macrophages in gingival tissues (DAPI: blue). (f1)–(f3) Micro-CT quantification: Vertical bone resorption (cemento-enamel junction to alveolar bone crest (CEJ-BC) distance); BMD; and bone volume fraction (BV/TV). (g1) and (g2) Histomorphometric analysis: $TRAP^+$ osteoclasts/field; and inflammatory infiltrates in junctional epithelium. Abbreviations: Lig, ligation; HA, hydroxyapatite. Data: mean ± s.e.m. ($n = 6$); $^{***}P < 0.001$, $^{**}P < 0.01$, $^{*}P < 0.05$, ns: not significant (one-way ANOVA with Tukey's test).

stress in modulating inflammatory responses and immune regulation [44]. Our results from flow cytometry and fluorescence imaging revealed that PLCL-nHA significantly reduced intracellular ROS level compared to the LPS group (Fig. 4(g) and Fig. S3(b) in the ESM), with 2',7'-dichlorodihydrofluorescein diacetate (DCFH-DA) fluorescence intensity decreased by 15.4% ($^{**}P < 0.01$) (Fig. 4(i)), accompanied by high expression of antioxidant genes and proteins (Figs. 4(h) and 4(j)). Ameliorating cellular oxidative stress promotes inflammation resolution and enhances tissue repair [45, 46].

To dissect the molecular circuitry through which PLCL-nHA attenuates inflammation and oxidative damage while steering macrophage polarization, we performed RNA sequencing on LPS-stimulated human acute monocytic leukemia cell line (THP-1) macrophages treated with PLCL-nHA extracts (Fig. 5(a)). Pathway and Gene Oncology (GO) analysis revealed significant downregulation of critical pro-inflammatory pathways—including nucleotide-binding oligomerization domain (NOD)-like receptor signaling, TNF signaling, and IL-17 signaling pathways—in PLCL-nHA-treated groups compared to LPS controls (Figs. 5(b) and 5(c)), corroborated by Gene Set Enrichment Analysis (GSEA) showing preferential depletion of inflammatory gene sets (NOD-

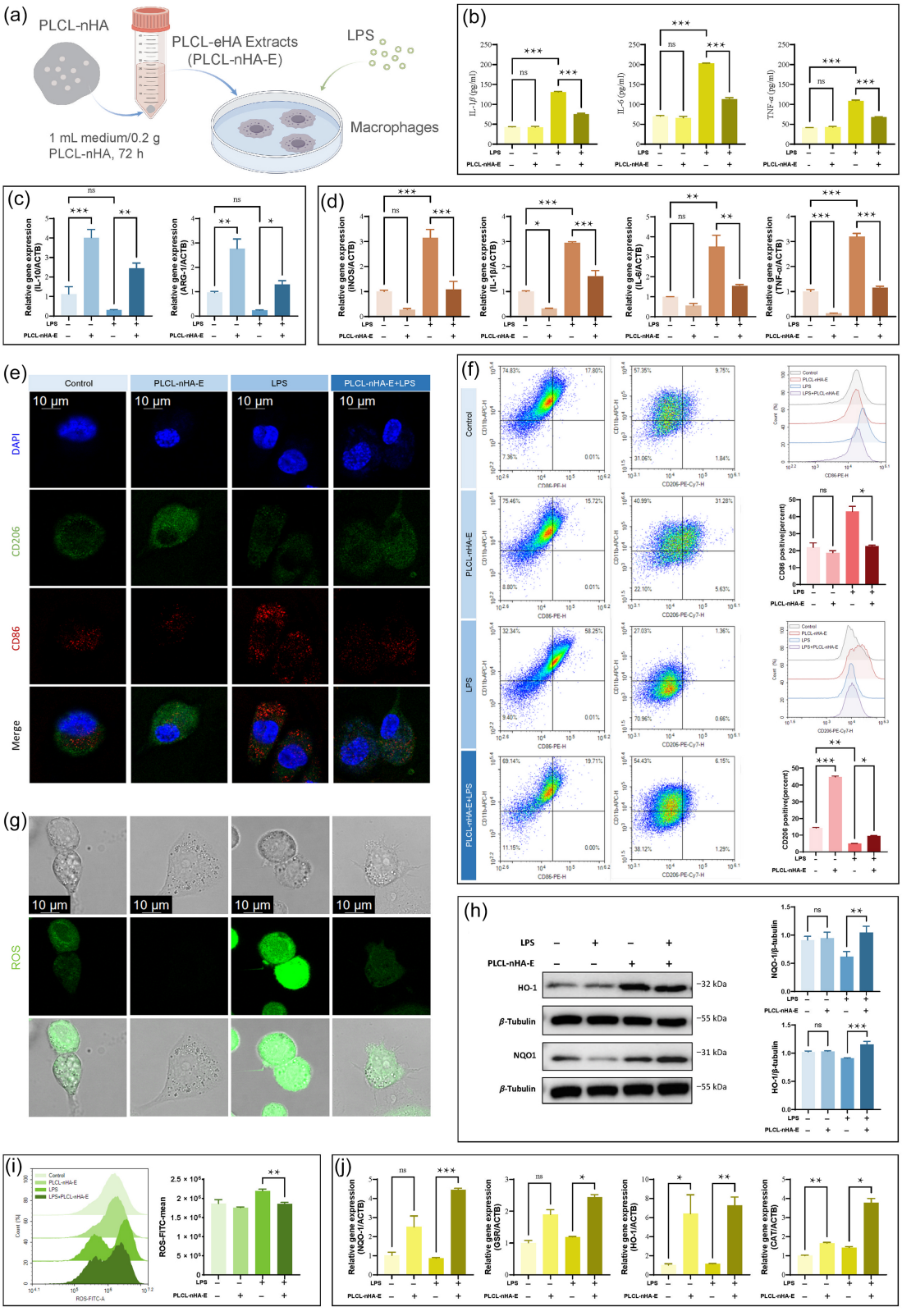

Figure 4 Mechanistic validation of immunomodulatory and antioxidant effects in THP-1 macrophages. (a) Experimental schematic: Preconditioning protocol with PLCL-nHA extracts (PLCL-nHA-E) on PMA-differentiated THP-1 macrophages under LPS-induced inflammatory challenge. (b) Cytokine profiling: ELISA quantification of pro-inflammatory cytokines (IL-1β, IL-6, and TNF-α) in supernatants; (c) qPCR analysis showing M2 polarization (IL-10, ARG1) and (d) M1 suppression (iNOS, IL-1β, IL-6 and TNF-α). (e) Phenotypic characterization: Confocal microscopy (60×) of M1/M2 surface markers (CD86: red/CD206: green, DAPI: blue). (f) Flow cytometry quantification. (g) Oxidative stress modulation: confocal imaging (60×) and (i) flow cytometric quantification of cellular ROS. Antioxidant pathway activation: (h) Western blot analysis of HO-1 and NQO-1, (j) qPCR of antioxidant genes: NQO-1, glutathione reductase (GSR), HO-1 and CAT. Data: mean ± s.e.m. ($n = 3$); $^{***}P < 0.001$, $^{**}P < 0.01$, $^{*}P < 0.05$, ns: not significant (one-way ANOVA).

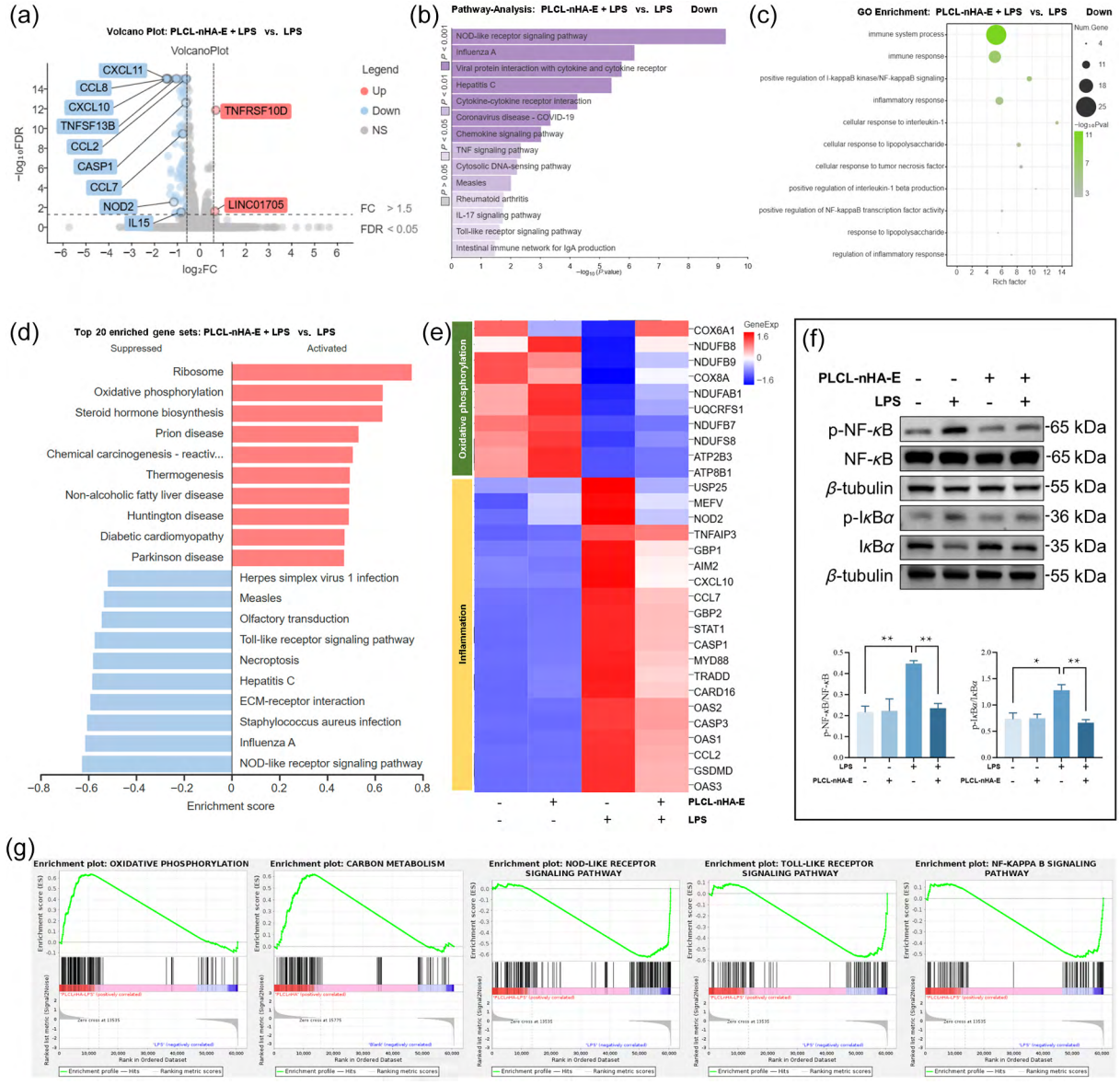

Figure 5 Transcriptomic sequencing reveals metabolic-immune crosstalk. (a) Volcano plot of differentially expressed genes (DEGs) between PLCL-nHA+LPS and LPS groups (|$\log_2$Fold Change| > 1, FDR < 0.05); (b) KEGG pathway enrichment analysis of DEGs. (c) GO biological process enrichment; (d) GSEA results showing top 20 enriched gene sets (red: activated in PLCL-nHA+LPS; blue: suppressed). (e) Heatmap of DEGs annotated with oxidative phosphorylation (green) and inflammation-related genes (yellow); (f) NF-κB pathway activation: Western blot of key proteins and quantification; (g) GSEA enrichment plots: Oxidative phosphorylation, carbon metabolism, NOD-like receptor pathway, Toll-like receptor signaling and NF-κB pathway. Data: mean ± s.e.m. (n = 3); ***P < 0.001, **P < 0.01, *P < 0.05, ns: not significant. PLCL-nHA-E: PLCL-nHA extracts.

like receptor (NLR): Normalized Enrichment Score (NES) = −1.537, Nominal (NOM) P-val < 0.01; TLR: NES = −1.31, NOM P-val < 0.05) (Fig. 5(d)). GO functional annotation analysis also revealed possible inhibition of the NF-κB signaling pathway, given its pivotal role in inflammatory responses, Western blot analysis further confirmed attenuated activation of this pathway in LPS-stimulated conditions following PLCL-nHA treatment (Fig. 5(f)).

Simultaneously, GSEA revealed significant enrichment of energy metabolism- and mitochondrial function-related gene sets (oxidative phosphorylation (OXPHOS): NES = 1.592, NOM P-val < 0.001; carbon metabolism: NES = 1.401, NOM P-val < 0.05) in upregulated genes from the PLCL-nHA group (Figs. 5(e) and 5(g)). The marked upregulation of oxidative phosphorylation implies that PLCL-nHA may promote mitochondrial metabolic reprogramming, enhance aerobic respiration, and regulate cellular energy status.

Given the close relationship between cellular metabolism and inflammatory regulation, activated macrophages shift toward glycolysis during pro-inflammatory polarization, while mitochondrial function transitions from adenosine triphosphate (ATP) synthesis to ROS production to sustain inflammatory states [47]. Enhanced oxidative phosphorylation may not only improve mitochondrial function and reduce oxidative stress but also promote macrophage polarization toward anti-inflammatory phenotypes through metabolic regulation [48].

2.4 PLCL-nHA preserves mitochondrial function

To further validate the RNA sequencing findings indicating

upregulation of aerobic metabolism-associated genes in PLCL-nHA-treated groups, we systematically investigated mitochondrial bioenergetics and oxidative phosphorylation dynamics in macrophages.

LPS stimulation significantly increased mitochondrial superoxide level ($^{***}P < 0.001$) and reduced the mitochondrial membrane potential ($^{***}P < 0.001$) [49, 50], as indicated by MitoSOX™ and tetramethylrhodamine methyl ester (TMRM) fluorescence imaging and flow cytometry. However, treatment with PLCL-nHA reduced mitochondrial superoxide level ($^{***}P < 0.001$) and preserved $\Delta\Psi m$ by 27.1% compared to the LPS group (Figs. 6(a) and 6(b), and Fig. S3(c) in the ESM).

Mitochondria serve as the primary site for oxidative phosphorylation, efficiently generating cellular energy through ATP synthesis [51]. To assess functional alterations, mitochondrial stress tests were performed. LPS treatment significantly impaired mitochondrial respiratory parameters, including basal, maximal and spare respiration capacity ($^{***}P < 0.001$) (Fig. 6(c)). PLCL-nHA-treated macrophages showed increased oxygen consumption rate (OCR) under basal and maximal respiration conditions, while extracellular acidification rate (ECAR), indicative of glycolytic activity, was decreased compared to the LPS group ($^{**}P < 0.01$) (Fig. 6(c)). Consistent with the aforementioned changes, metabolic analysis revealed that LPS treatment significantly reduced intracellular ATP levels while increasing extracellular lactate accumulation, PLCL-nHA intervention effectively reversed these metabolic perturbations, restoring ATP content ($P < 0.01$) and suppressing lactate overproduction ($P < 0.005$) (Fig. 6(d)), demonstrating its capacity to rebalance energy metabolism under inflammatory conditions.

Pharmacological inhibition of the mitochondrial pyruvate carrier with UK5099 (10 μM) [52] completely abolished the metabolic regulatory effects of PLCL-nHA extracts, as indicated by the loss of ATP restoration, reversal of lactate-associated metabolic changes, and reactivation of inflammatory signaling (Figs. 6(d), 6(e1)–6(e3), and 6(f)). Importantly, UK5099 alone did not affect macrophage viability or basal inflammatory gene expression (Fig. S4 in the ESM), identifying mitochondrial pyruvate metabolism as a key mechanistic link between metabolic reprogramming and inflammatory suppression. Given the central role of mitochondria in coordinating cellular metabolism and inflammatory signaling [53–55], these findings align with established paradigms in which inflammatory activation disrupts mitochondrial homeostasis, promotes ROS accumulation, and amplifies NF-κB–dependent responses, whereas restoration of mitochondrial oxidative metabolism supports anti-inflammatory phenotypes [56–58].

Fractionation analysis further showed that the soluble fraction, containing physiologically relevant concentrations of lactate [59], accounted for most of the monocarboxylate transporter 1 (MCT1)-dependent immunometabolic effects, including enhanced expression of M2-associated markers and suppression of pro-inflammatory cytokines (Fig. S5 in the ESM). In line with prior studies, lactate uptake via MCT1 can support tricarboxylic acid cycle (TCA) cycle activity and oxidative phosphorylation [20], thereby restraining glycolysis-associated inflammatory programs. In addition to its metabolic role, lactate has been reported to attenuate NF-κB–dependent transcription through receptor- and metabolism-coupled pathways, such as G protein-coupled receptor 81 (GPR81)-associated signaling [20], collectively favoring an anti-inflammatory state. By contrast, the particulate nHA-containing fraction exerted a weaker but reproducible immunomodulatory effect, consistent with previous reports that nanoscale hydroxyapatite can mediate M2 macrophage polarization [60]. Although the precise molecular mechanisms remain incompletely defined, existing evidence suggests that nHA may contribute to macrophage reprogramming by modulating mitochondrial function [61], scavenging ROS via surface electron-donating properties [62], and exploiting its chemical and physical similarity to natural bone [60]. In our system, nHA also limited excessive acidification during material degradation (Fig. S1 in the ESM), which may indirectly support mitochondrial stability and inflammatory resolution. Taken together, these findings identify mitochondrial pyruvate metabolism as a central node in PLCL-nHA–induced macrophage reprogramming, integrating soluble metabolic cues and particulate material signals to promote a shift toward oxidative phosphorylation. Notably, this shift reflects enhanced mitochondrial metabolic utilization and functional recovery rather than confirmed induction of mitochondrial biogenesis, as canonical biogenesis regulators were not directly examined in the present study. This metabolic state is associated with reduced NF-κB activation and attenuation of inflammation-associated oxidative stress, providing a mechanistic basis for the immunomodulatory effects observed *in vitro*.

2.5 PLCL-nHA accelerates alveolar bone regeneration in rats under inflammation

To assess the regenerative potential of PLCL-nHA for alveolar bone defect due to periodontitis, an inflammatory periodontal bone defect model in rat was employed (Fig. 7(a)) [63]. The ligated bone defects treated with PLCL-nHA (LD+ PLCL-nHA group) were compared to control groups, including untreated ligated defects (LD) and ligated defects treated with HA (LD+HA group). The PLCL composite demonstrated superior clinical handling characteristics, particularly its exceptional moldability that enabled precise adaptation to complex bone defect morphologies. In contrast, HA particles exhibited poor structural integrity, being prone to intraoperative dispersion and postoperative washout, with residual granules frequently retained within soft tissue flaps.

Micro-CT analysis with three-dimensional reconstruction analysis demonstrated that the LD+PLCL-nHA group achieved near-physiological bone morphology restoration at 6 weeks post-implantation, closely resembling healthy controls. While the LD+HA group exhibited partial defect filling, radiolucent halos surrounding the graft particles suggested compromised osseointegration. The ligated defect group retained substantial unhealed areas (Fig. 7(b)). Quantitative analyses showed significantly less depth of bone defect, higher BV/TV and bone mineral density (BMD) in the LD+PLCL-nHA group compared to the ligated defect group and LD+HA groups ($P < 0.05$) (Fig. 7(g)). In addition, *in vitro* osteogenic assays demonstrated that PLCL-nHA directly enhanced the osteogenic differentiation of periodontal ligament cells (PDLCs) (Fig. S6 in the ESM), consistent with previous reports highlighting the importance of mitochondrial metabolic support for PDLC osteogenesis [64]. Notably, under LPS-induced inflammatory conditions, PLCL-nHA further promoted osteogenic differentiation through an indirect material–macrophage–PDLC crosstalk (Fig. S7 in the ESM). Given the immune-driven nature of periodontal bone loss, these findings suggest that while PLCL-nHA exerts a direct pro-osteogenic effect on PDLCs, its immunometabolic regulation of macrophages

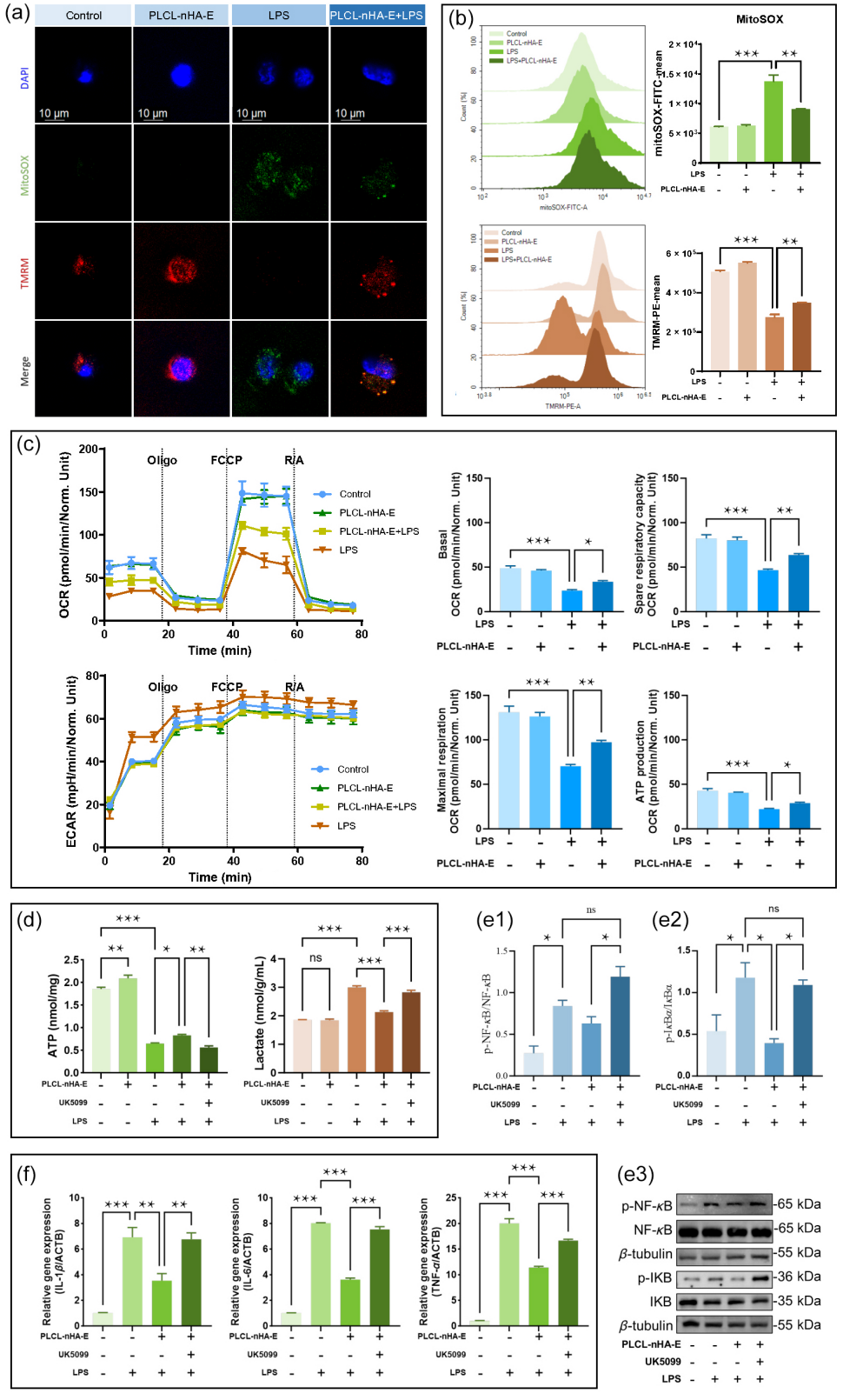

Figure 6 Mitochondrial functional analysis and metabolic mechanism validation. (a) Confocal microscopy (60×) of TMRM (red) and MitoSOX (green) staining illustrating membrane potential (ΔΨm) and mitochondrial superoxide levels. (b) Flow cytometric quantification. (c) Mitochondrial stress test (seahorse XF analyzer): OCR profiles under sequential injections: Oligomycin (ATP synthase inhibitor, 1 μM), carbonyl cyanide p-trifluoromethoxyphenylhydrazone (FCCP) (uncoupler, 0.5 μM), Rotenone/Antimycin A (complex I/III inhibitors, 0.5 μM); ECAR reflecting glycolytic flux; bioenergetic parameters: basal respiration, spare respiratory capacity, maximal respiration, and ATP-linked respiration. (d) Metabolite quantification: intracellular ATP levels and lactate secretion; UK5099, mitochondrial pyruvate carrier inhibitor. Mechanistic blockade with UK5099 abolished material-induced immunomodulation: (e) Western blot of key protein in NF-κB pathway activation. (f) qPCR of IL-1*β*, IL6 and TNF-*α*. Data: mean ± s.e.m. ($n = 3$); ***$P < 0.001$, **$P < 0.01$, *$P < 0.05$, ns: not significant (one-way ANOVA). PLCL-nHA-E, PLCL-nHA extracts.

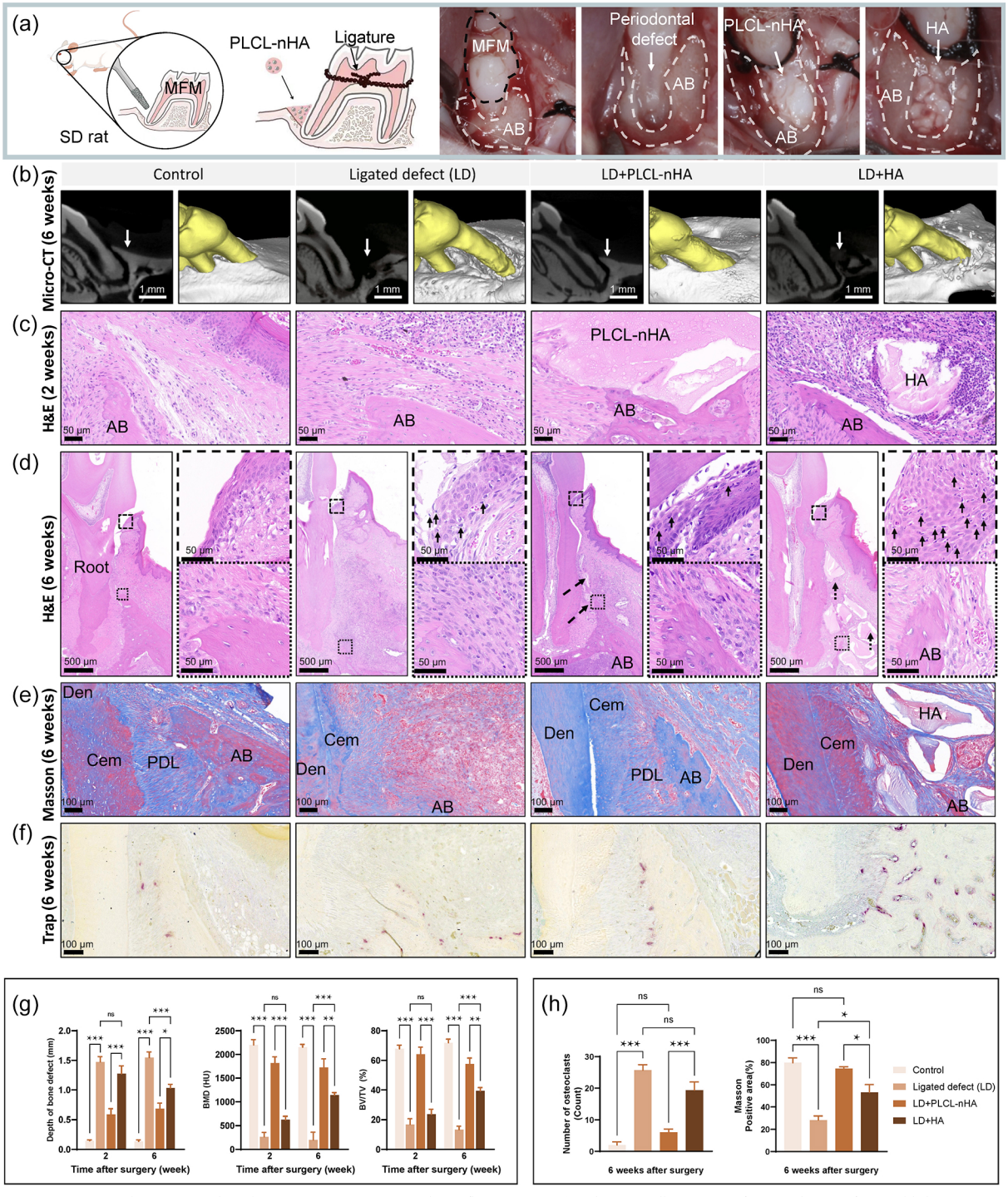

Figure 7 PLCL-nHA accelerates periodontal regeneration in rats under inflammation. (a) Schematic illustration of surgical steps for establishing a standardized periodontal bone defect model at the mesial aspect of rat maxillary first molars; intraoperative photographs demonstrating PLCL-nHA and HA graft placement. (b) Micro-CT evaluation at 6 weeks post-operation with sagittal views with arrow-indicated defect areas and 3D-reconstructed alveolar bone morphology. (c) Histological characterization via H&E staining at 2nd week (material-bone integration) and (d) 6 weeks (epithelial inflammatory infiltrates/osteoblast distribution at bone crest), supplemented by (e) Masson's trichrome staining (collagen regeneration) and (f) TRAP staining (osteoclast activity quantification); (g) quantitative micro-CT analyses including vertical bone defect depth (distance from defect apex to theoretical alveolar crest), BMD, and BV/TV. (h) histomorphometric quantification of osteoclast numbers (TRAP staining) and collagen deposition ratio (Masson-positive area). Data: mean ± s.e.m. (n = 6); ***P < 0.001, **P < 0.01, *P < 0.05, ns: not significant (one-way ANOVA). MFM: maxillary first molar; AB, alveolar bone; Cem, cementum; Den, dentin.

represents a dominant and disease-relevant mechanism amplifying osteogenesis in an inflammatory microenvironment.

Histological analysis at 2nd week post-surgery revealed superior osseointegration in the LD+PLCL-nHA group, where bone intimately interfaced with PLCL-nHA and infiltrated its porous architecture. In contrast, LD+HA grafts exhibited peri-implant inflammatory cell encapsulation (Figs. 7(c) and 7(d)). By 6 weeks, PLCL-nHA-mediated bone remodeling culminated in functionally

oriented bony septa with regenerated Sharpey's fibers (Masson's trichrome: higher collagen fiber density than ligated defect group and LD+HA groups) (Figs. 7(e) and 7(h)). TRAP staining confirmed material-driven osteoclast inhibition, substantiating its dual capacity for osteogenesis promotion and catabolic suppression (Figs. 7(f) and 7(h)).

Immunofluorescence quantification revealed a pronounced M2 macrophage polarization in the LD+PLCL-nHA group, whereas ligated defect group and LD+HA group predominantly exhibited pro-inflammatory M1 polarization (Figs. 8(a), 8(d1), and 8(d2)). This immunomodulatory advantage was paralleled by attenuated oxidative damage, as evidenced by lower 8-OHdG positive fluorescence area in the LD+PLCL-nHA group (Figs. 8(b) and 8(e)). Ultrastructural analysis via TEM further demonstrated the LD+PLCL-nHA's mitochondrial protective capacity: preserved cristae density contrasted sharply with the ligated defect and LD+HA groups, which exhibited hallmark pathologies including matrix vacuolization, cristae fragmentation, and outer membrane rupture (Fig. 8(c)) (damaged mitochondria: 45.2% ± 5.1% vs. 74.8% ± 8.3% in the ligated defect group, $P < 0.01$) (Fig. 8(f)). Consistent with this, metabolic assays demonstrated a reduction in gingival lactate levels ($P < 0.01$) and an attenuation of ATP depletion in LD+PLCL-nHA group (Figs. 8(g1) and 8(g2)). The observed mitochondrial pathologies in ligated defect and HA groups (cristae fragmentation, matrix vacuolization) mirror the metabolic crisis typical of inflammatory cells, where glycolytic reprogramming sustains pro-inflammatory cytokine production [65]. In contrast, PLCL-nHA drives the transition from glycolysis toward OXPHOS to minimize mitochondrial stress and mtROS leakage, in consistent with the metabolic reprogramming observed *in vitro*, thereby protecting mitochondrial integrity which is also energetically unfavorable for M1 polarization but conducive to M2 differentiation [66]. Molecular analysis further correlated these phenotypic improvements with diminished pro-inflammatory cytokine secretion (IL-1β, IL-6, and TNF-α) (Figs. 8(h1)–8(h3)).

The integrated findings from this study delineate a multifaceted mechanism through which the PLCL-nHA biomaterial orchestrates periodontal tissue repair, synergistically coupling immunomodulation, oxidative homeostasis, and mitochondrial protection. The pronounced M2 macrophage polarization observed in PLCL-nHA group aligns with its anti-inflammatory and pro-regenerative phenotype, as M2 macrophages are known to secrete trophic factors (e.g., transforming growth factor-beta (TGF-β), IL-10) that suppress osteoclastogenesis and promote collagen matrix stabilization [67, 68]. This immunomodulatory effects of PLCL-nHA help prevent excessive inflammation and edema, which may explain the observed shifts in the local microbiota shown in Fig. 2. Although microbiome dysbiosis is a driving factor in periodontitis, the present study focuses on immune modulation rather than direct antibacterial activity, reflecting the intended role of PLCL-nHA as a regenerative graft material. However, antibacterial strategies remain essential for periodontal therapy and may be highly complementary to immunomodulatory biomaterials in future combined treatment paradigms [69].

Notably, the superiority of PLCL-nHA over HA—a widely used graft material—in all evaluated parameters (M2 polarization, mitochondrial integrity, NF-κB inhibition) highlights the limitations of passive osteoconductive materials in resolving immune-metabolic dysregulation. While HA provides structural scaffolding, it fails to actively modulate the inflammatory microenvironment, allowing persistent M1 activation and oxidative damage [70]. In contrast, PLCL-nHA incorporates material-derived metabolic and immunomodulatory cues that collectively favor mitochondrial oxidative metabolism and inflammatory resolution within the pathological niche.

3 Conclusions

In conclusion, our findings highlight the translational potential of PLCL-nHA in periodontal regeneration under inflammatory conditions. By attenuating local inflammation and supporting functional tissue reconstruction, as evidenced by improved Sharpey's fiber attachment, PLCL-nHA addresses a key challenge in periodontal therapy, where persistent immune dysregulation and microbial stress often compromise regenerative outcomes. Future studies should further evaluate long-term functional recovery and clarify the cell-type specificity of mitochondrial metabolic regulation *in vivo*, which remains an important direction beyond the scope of the present work.

4 Experimental

4.1 Synthesis and characterization of a PLCL-nHA bone substitute

PLCL-nHA composites were synthesized via a three-step protocol. Hydroxyapatite nanoparticles were prepared through a hydrothermal method. Calcium nitrate tetrahydrate and ammonium hydrogen phosphate solutions (Ca/P = 1.67) were mixed under pH 10 adjusted by $NH_3{\cdot}H_2O$. The mixture underwent hydrothermal treatment at 140 °C for 24 h, followed by washing, freeze-drying, and sieving (< 75 μm). Poly(L-lactic acid-co-ε-caprolactone) was synthesized via ring-opening polymerization (ROP). L-lactide and ε-caprolactone (1:1 molar ratio) were copolymerized using trimethylolpropane as the trifunctional initiator and stannous octoate ($Sn(Oct)_2$) as the catalyst at 130 °C for 48 h under vacuum. The product was purified by precipitation in cold ethanol. PLCL and nHA (1:1 w/w) were blended in chloroform, ultrasonicated for 30 min, and cast into films via solvent evaporation. The composite was vacuum-dried at 70 °C for 24 h and sterilized by Co^{60} γ-irradiation (25 kGy).

Physicochemical characterization included SEM (Hitachi SU8010) to evaluate surface morphology before and after 4-week degradation in simulated body fluid (SBF), FTIR (Nicolet iS50) for chemical structure analysis (4000–500 cm^{-1}), and mechanical testing (Instron 5567) to measure compressive strength and elastic modulus at 25 and 37 °C. The pH of the degradation medium was also measured at days 1, 3, 5 and 7 using a calibrated digital pH meter (Mettler Toledo, Zurich, Switzerland). Hydrophilicity was assessed via water contact angle measurements (OCA20, DataPhysics) using 5 μL deionized water droplets. Material extracts were prepared according to ISO 10993-12 (1 mL medium/0.2 g material, 72 h). The collected extracts were centrifuged to remove insoluble debris, and nanoparticle tracking analysis (NTA, NanoSight NS300, Malvern Panalytical) was performed to characterize particle size distribution in the extracts. The extracts were further centrifuged at 15,000×*g* for 30 min to separate the supernatant (soluble fraction, SF) and the pellet (particulate fraction, PF), which was resuspended in an equal volume of fresh medium. In addition, lactate concentration in the extracts was quantified using a lactate assay kit (Beyotime, Beijing, China).

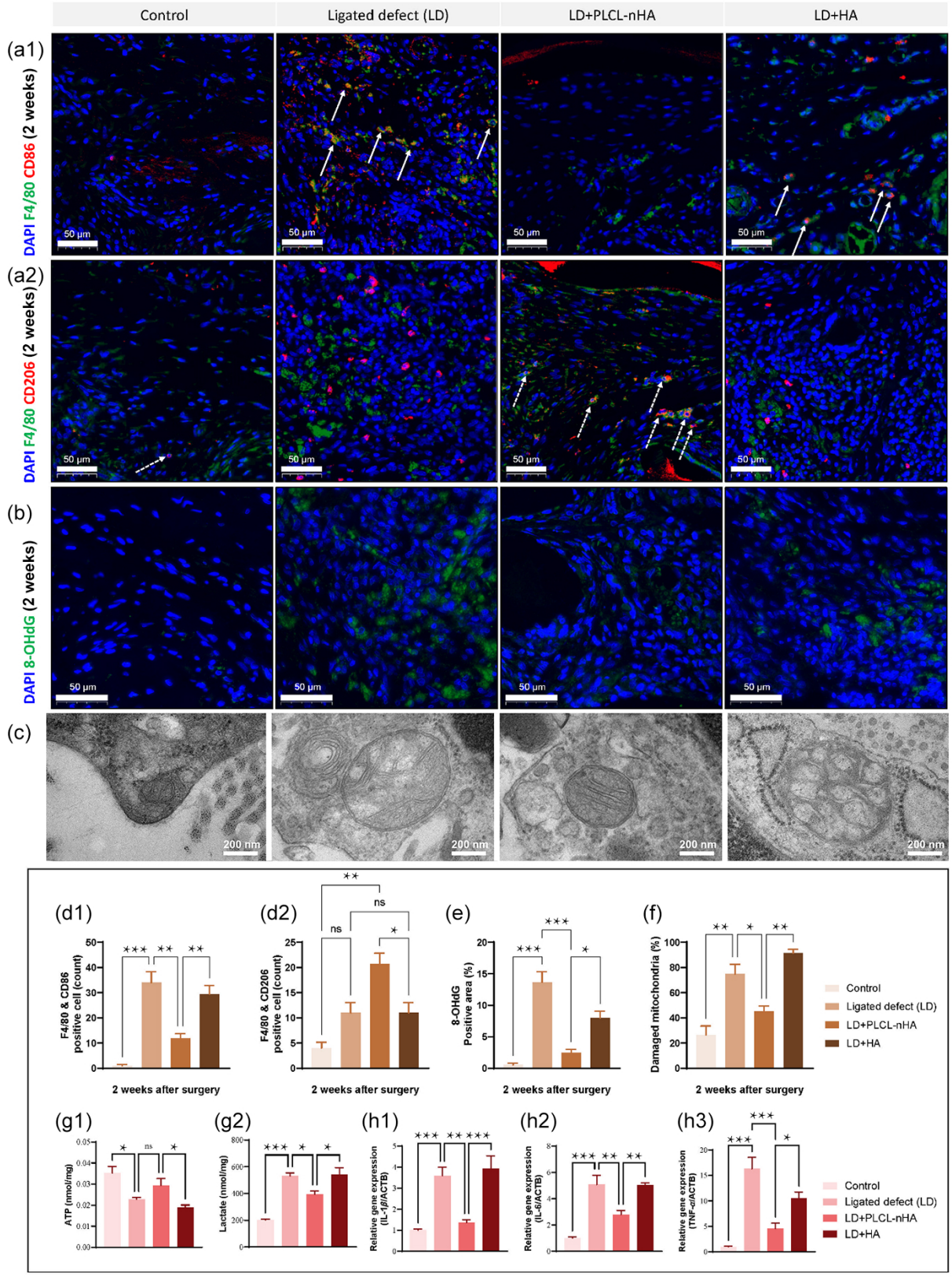

Figure 8 Multimodal analysis of immunomodulation and mitochondrial protection in periodontal tissues. (a) Immunofluorescence staining of rat gingival tissues demonstrates macrophage phenotypic distribution through co-localization analysis ($CD86^+/CD206^+$: red, $F4/80^+$: green, DAPI: blue). (b) Oxidative DNA damage is visualized via 8-OHdG immunohistochemical staining, while (c) TEM (scale bar: 200 nm) reveals mitochondrial ultrastructural integrity in stromal cells. Quantitative analyses include (d) macrophage polarization indices, (e) 8-OHdG intensity, and (f) percentage of damaged mitochondria. (g1) ATP levels (nmol/mg protein), (g2) lactate content (nmol/mg protein) and (h) qPCR quantification of pro-inflammatory mediators in gingival tissues from rats. Data: mean ± s.e.m. ($n = 3$); $^{***}P < 0.001$, $^{**}P < 0.01$, $^{*}P < 0.05$, ns: nonsignificant (one-way ANOVA).

4.2 *In vitro* biocompatibility and immunomodulation

hPDLCs (EallBio, Beijing, China) and THP-1 monocytes (EallBio) were cultured in α-MEM or RPMI 1640 medium (10% fetal bovine serum (FBS), 1% Penicillin-Streptomycin) in an incubator at 37 °C with 5% CO_2. THP-1 cells were differentiated into M0 macrophages using 100 ng/mL phorbol 12-myristate 13-acetate (PMA, Sigma) for 24 h. Material extracts were prepared per ISO 10993-12:2021. For cytotoxicity assays, hPDLCs between passages 4 and 5 were treated with extracts for either 24, 48 or 72 h, and viability was assessed via CCK-8 (Beyotime, Beijing, China) and live/dead staining (Calcein-AM/propidium iodide (PI), Beyotime, Beijing, China). Fluorescent images were captured using a fluorescence microscope (Olympus, Japan) to distinguish live cells (green fluorescence) and dead cells (red fluorescence). Samples were also analyzed using *NovoCyte* flow cytometer (*NovoCyte*, ACEA, USA). The proportion of calcein-AM and PI-positive cells was calculated to quantify live and dead cells.

Macrophage polarization studies involved treating THP-1-derived M0 cells (100 ng/mL phorbol 12-myristate 13-acetate (PMA) for 24 h) with PLCL-nHA extracts for 24 h, followed by LPS (1 μg/mL) stimulation. Cytokine levels (IL-1β, TNF-α, IL-6) in supernatants were quantified via ELISA (Solarbio, Beijing, China). Total RNA was extracted using RNAeasy™ Animal RNA Isolation Kit (Beyotime, Shanghai, China) and reverse-transcribed into cDNA, and quantitative PCR (qPCR) was performed to evaluate the expression of inflammatory (IL-1β, TNF-α, IL-6), anti-inflammatory (ARG-1, IL-10), and oxidative stress markers (heme oxygenase-1 (HO-1), NAD(P)H: quinone oxidoreductase 1 (NQO1), catalase (CAT)) normalized to actin beta (ACTB) using the $2^{-\Delta\Delta Ct}$ method (see primers in the ESM). RNA integrity was verified using the Agilent 2200 system (RNA integrity number (RIN) ≥ 7.0). Poly-A mRNA was enriched from 1 μg total RNA via oligo(dT) beads, fragmented, and processed into strand-specific libraries using the VAHTS Universal V6 Kit (Vazyme). Libraries were sequenced on the DNBSEQ-T7 platform (150 bp paired-end). Clean reads were aligned to GRCh38 (STAR v2.7.10a), and differential expression was analyzed with EBSeq (|fold change| > 1.5, false discovery rate (FDR) < 0.05). Functional enrichment (GO, Kyoto Encyclopedia of Genes and Genomes (KEGG)) was assessed via Fisher's exact test ($P < 0.05$).

Flow cytometry (NovoCyte 3000) with APC-CD11b, PE-CD86, and PE/Cy7-CD206 antibodies (BioLegend) was used to quantify M1/M2 polarization. To visualize M1 and M2 markers, cells were fixed with 4% paraformaldehyde, permeabilized with 0.1% Triton X-100, and blocked with 5% bovine serum albumin (BSA). Samples were incubated with primary antibodies targeting M1 marker CD86 (BioLegend, USA) and M2 markers CD206 (BioLegend, USA), followed by corresponding secondary antibodies conjugated with fluorophores. 4',6-diamidino-2-phenylindole (DAPI) was used to stain nuclei. Fluorescent images were captured using an Olympus inverted fluorescence microscope.

In vitro osteogenic differentiation was assessed using a Transwell co-culture system with THP-1 macrophages and hPDLCs. Cells were treated with PLCL-nHA extract and/or LPS (1 μg/mL) in osteogenic induction medium (alpha minimum essential medium (α-MEM) + 10% FBS, 100 nM dexamethasone, 10 mM β-glycerophosphate, 50 μM ascorbate). After 48 h co-culture, osteogenic genes (Runt-related transcription factor 2 (RUNX2), osteocalcin (OCN), alkaline phosphatase (ALP), Osterix) were analyzed by qPCR. ALP activity was quantified at 72 h (Beyotime), and mineralization nodules were stained with Alizarin Red (Beyotime) at day 14 (ImageJ analysis).

4.3 Effects of PLCL-nHA on mitochondrial function

Mitochondrial function was assessed using DCFH-DA (intracellular ROS level), TMRM (membrane potential) and MitoSOX™ Red (mitochondrial ROS) probes, with fluorescence quantified via confocal microscopy (Leica SP8) and flow cytometry. Oxygen consumption and extracellular acidification rates OCR and ECAR were measured using a Seahorse XF Analyzer (Agilent). Macrophages were seeded in XF96 plates and sequentially exposed to oligomycin (1 μM), FCCP (1 μM), and rotenone/antimycin A (0.5 μM each) to analyze mitochondrial respiration and glycolytic activity. For mechanistic validation, UK5099 (10 μM, Sigma-Aldrich) and AZD3965 (100 nM, Sigma-Aldrich) were used to inhibit mitochondrial pyruvate carrier and MCT1, respectively, with 1 h pretreatment. Data were normalized to protein content. Metabolic profiling also included ATP and lactate measurements (Beyotime).

Proteins were lysed in radioimmunoprecipitation assay buffer (RIPA, Beyotime) with protease/phosphatase inhibitors (Thermo Fisher), quantified via bicinchoninic acid (BCA) assay (Beyotime), electrophoresed, and transferred to polyvinylidene difluoride (PVDF) membranes (Millipore). Membranes were incubated with primary antibodies (HO-1, NQO-1, NF-κB pathway markers, β-Tubulin; Abmart) and horseradish peroxidase (HRP)-conjugated secondaries (Abmart). Signals were detected by enhanced chemiluminescence (ECL, Beyotime) and analyzed with ImageJ.

4.4 *In vivo* ligation induced periodontitis model

For the mouse model, 8-week-old male C57BL/6J mice (Beijing Vital River Laboratory, Beijing, China) were ligated with 5-0 silk sutures around maxillary second molars to induce periodontitis. PLCL-nHA (0.5 × 0.5 × 0.5 mm^3) or HA (Bio-Oss®, Geistlich, Switzerland) was implanted into periodontal pockets at 2 weeks post-ligation. Another two weeks after material placement, the mice were sacrificed for further analysis. Silk ligatures were utilized to collect sulcular microorganisms from the ligated second molars. A 5 mm silk thread was tied in the gingival sulcus of the maxillary first molar for 10 min before removal. DNA was extracted from the ligatures using the E.Z.N.A.®. Soil DNA Kit (Omega Bio-tek, USA) according to the manufacturer's instructions. The V3–V4 hypervariable regions of the bacterial 16S rRNA gene were amplified using the universal primers 338F (5'-ACTCCTACGGGAGGCAGCAG-3') and 806R (5'-GGACTACNNGGGTATCTAAT-3'). Sequencing of all samples was conducted on an Illumina Miseq/Nextseq 2000/Novaseq 6000 platform (Illumina, USA) at Beijing Allwegene Technology Co., Ltd. Post-sequencing, image analysis, base calling, and error correction were carried out using the Illumina Analysis Pipeline Version 2.6 (Illumina, USA). Sequence data have been deposited in the NCBI BioProject database under accession number PRJNA1275906.

Micro-CT (Siemens Inveon, 9.23 μm resolution) quantified vertical bone loss (CEJ to bone crest at four sites) and bone parameters (BMD; BV/TV) in cylindrical ROIs (defined as the bone tissue surrounding the second molar excluding the teeth). Maxillary tissue sections were made in the mesio-distal direction and stained

with H&E staining and TRAP staining to evaluate inflammation, collagen deposition, and osteoclast activity. The sample size (n = 6 per group) was determined through a priori power analysis (GPower 3.1; α = 0.05, β = 0.2, effect size d = 1.8) based on pre-experimental bone height data, ensuring statistical power (> 80%) while adhering to the 3R principles. This protocol was approved by the Institutional Animal Ethics Committee of Peking University Health Science Center (No. DLASBD0730).

4.5 *In vivo* inflammatory periodontal bone defect model

8-week-old specific pathogen free (SPF) male Sprague-Dawley (SD) rats (Beijing Vital River Laboratory, Beijing, China) were used. After systemic anesthesia, incision and flap elevation, an intrabony defect (1.5 × 1.5 × 1 mm^3; depth × length × width) was created using a diamond bur, followed by PLCL-nHA or HA (Bio-Oss®, Geistlich, Switzerland) implantation [63]. Silk ligatures (5-0) were placed around the cervical regions of the maxillary first molars to induce periodontal inflammation. The maxillary bones were harvested at 2/6 weeks for further investigation. Radiographic analysis included the depth of bone defect (measured from the assumed bone crest to the bottom of the defect), BMD and BV/TV of region of interest (ROI, triangular bone defect area created by resection in mesial-distal direction, comprising a stack of 50 sections). Decalcified maxillae were paraffin-embedded, sectioned (4 μm), and stained with H&E (inflammatory cell quantification), Masson's trichrome (collagen deposition), and TRAP (osteoclast counting). For mitochondrial ultrastructure analysis, gingival tissues were fixed in 2.5% glutaraldehyde, post-fixed in 1% osmium tetroxide, dehydrated in graded ethanol, embedded in epoxy resin, and sectioned (70 nm). Ultrathin sections were stained with uranyl acetate and lead citrate, then examined using a Hitachi HT7800 TEM (80 kV). The expression of IL-1β, IL-6, TNF-α (quantified by qPCR) in gingival tissues were analyzed using previously described methodologies. Gingival tissues were also homogenized, centrifuged (12,000 rpm, 4 ℃, 5 min), and supernatants assayed for ATP/lactate using commercial kits (Beyotime). BCA assays normalized data to total protein content.

The sample size (n = 6 per group) was determined through a priori power analysis (GPower 3.1; α = 0.05, β = 0.2, effect size d = 3.14) based on residual bone defect depth data from pilot studies (PLCL-nHA group: 0.7 ± 0.2 mm vs. ligated defect group: 1.5 ± 0.3 mm). This ensured statistical power > 99% while strictly adhering to the 3R principles. Ethical approval was granted by Animal Committee of Peking University Health Science Center (No. DLASBD0634).

Data from *in vitro* experiments (n = 3, biological replicates) and *in vivo* studies are presented as mean ± s.e.m. Statistical significance was determined by one-way ANOVA followed by Tukey-Kramer multiple comparison tests using GraphPad Prism v10.1.2, with P < 0.05 considered statistically significant.

Electronic Supplementary Material: Supplementary material (original Western blot (WB) images, and primer sequences) is available in the online version of this article at https://doi.org/10.26599/NR.2026.94908577.

Data availability

The sequencing data supporting the findings of this study have been deposited in the NCBI BioProject database under accession number PRJNA1275906. Other data generated or analyzed during this study are available from the corresponding author upon reasonable request.

Acknowledgements

The authors sincerely thank Dr. Yang Sun (Corliber Medical Device Co., Ltd., Shenzhen, China) for providing experimental materials and technical guidance. We are grateful to the editors and reviewers for their insightful suggestions. This work was supported by the National Key Research and Development Program of China (No. 2023YFC2506300), the National Natural Science Foundation of China (Nos. 82401105 and 82370956), and Shenzhen Science and Technology Research and Development Fund (No. JCYJ20190809165805604).

Declaration of competing interest

All the contributing authors report no conflict of interests in this work.

Author contribution statement

P. C.: Conceptualization, data curation, investigation, methodology, writing – original draft. N. L.: Conceptualization, data curation, formal analysis, investigation, methodology, validation, writing – original draft. Y.-q. L.: Data curation, formal analysis, software, visualization, writing – original draft. Y. Z.: Resources, writing – review & editing. P.-h. Z.: Investigation, validation. J. W.: Investigation, resources. Y. C.: Investigation, validation. C.-h. Y.: Formal analysis, software, visualization, writing – review & editing. L. C.: Funding acquisition, project administration, resources, supervision. Q.-x. L. (corresponding author): Conceptualization, funding acquisition, project administration, supervision, writing – review & editing. J. L.: Conceptualization, funding acquisition, methodology, project administration, supervision, writing – review & editing. All the authors have approved the final manuscript.

Informed consent

Not applicable.

Ethics statement

The animal experiments were carried out following the guidelines of the Institutional Animal Ethics Committee of Peking University Health Science Center (Ethical code: Nos. DLASBD0730 and DLASBD0634).

Use of AI statement

None.

References

[1] Papapanou, P. N.; Sanz, M.; Buduneli, N.; Dietrich, T.; Feres, M.; Fine, D. H.; Flemmig, T. F.; Garcia, R.; Giannobile, W. V.; Graziani, F. et al. Periodontitis: Consensus report of workgroup 2 of the 2017 world workshop on the classification of periodontal and peri-implant diseases and conditions. *J. Clin. Periodontol.* **2018**, *45*, S162–S170.

[2] Nascimento, G. G.; Alves-Costa, S.; Romandini, M. Burden of severe periodontitis and edentulism in 2021, with projections up to 2050: The

Global Burden of Disease 2021 study. *J. Periodontal Res.* **2024**, *59*, 823–867.
[3] Curtis, M. A.; Diaz, P. I.; Van Dyke, T. E. The role of the microbiota in periodontal disease. *Periodontol. 2000,* **2020**, *83*, 14–25.
[4] Hasturk, H.; Kantarci, A. Activation and resolution of periodontal inflammation and its systemic impact. *Periodontol. 2000*, **2015**, *69*, 255–273.
[5] Lin, D. P.; Li, L.; Sun, Y.; Wang, W. D.; Wang, X. Q.; Ye, Y.; Chen, X.; Xu, Y. Interleukin-17 regulates the expressions of RANKL and OPG in human periodontal ligament cells via TRAF6/TBK1–JNK/NF-κB pathways. *Immunology* **2015**, *144*, 472–485.
[6] Pan, W. Y.; Wang, Q. X.; Chen, Q. M. The cytokine network involved in the host immune response to periodontitis. *Int. J. Oral Sci.* **2019**, *11*, 30.
[7] Luchian, I.; Goriuc, A.; Sandu, D.; Covasa, M. The role of matrix metalloproteinases (MMP-8, MMP-9, MMP-13) in periodontal and peri-implant pathological processes. *Int. J. Mol. Sci.* **2022**, *23*, 1806.
[8] Cortellini, P.; Tonetti, M. S. Clinical concepts for regenerative therapy in intrabony defects. *Periodontol. 2000* **2015**, *68*, 282–307.
[9] Hiatt, W. H.; Schallhorn, R. G.; Aaronian, A. J. The induction of new bone and cementum formation: IV. Microscopic examination of the periodontium following human bone and marrow allograft, autograft and nongraft periodontal regenerative procedures. *J. Periodontol.* **1978**, *49*, 495–512.
[10] Jepsen, K.; Sculean, A.; Jepsen, S. Complications and treatment errors related to regenerative periodontal surgery. *Periodontol. 2000,* **2023**, *92*, 120–134.
[11] Gong, J. L.; Ye, C. X. Y.; Ran, J. H.; Xiong, X.; Fang, X. Y.; Zhou, X. M.; Yi, Y. T.; Lu, X.; Wang, J.; Xie, C. M. et al. Polydopamine-mediated immunomodulatory patch for diabetic periodontal tissue regeneration assisted by metformin-ZIF system. *ACS Nano* **2023**, *17*, 16573–16586.
[12] Huang, Y. J.; Tang, Y.; Zhang, R. Q.; Wu, X.; Yan, L.; Chen, X. L.; Wu, Q. Q.; Chen, Y. Y.; Lv, Y. T.; Su, Y. Role of periodontal ligament fibroblasts in periodontitis: Pathological mechanisms and therapeutic potential. *J. Transl. Med.* **2024**, *22*, 1136.
[13] Gao, S. T.; Li, H. H.; Li, Z. K.; Wang, H.; Li, X. Y.; Yang, S. Y.; Huang, L.; Zhang, B. P.; Zhang, K. L.; Tsoi, J. K. H. et al. Multifunctional injectable bioadhesive with toll-like receptor 4 and myeloid differentiation factor 2 antagonistic anti-inflammatory potential for periodontal regeneration. *ACS Nano* **2025**, *19*, 7098–7116.
[14] Watanabe, S.; Alexander, M.; Misharin, A. V.; Budinger, G. R. S. The role of macrophages in the resolution of inflammation. *J. Clin. Invest.* **2019**, *129*, 2619–2628.
[15] Yu, Y.; You, Z. Y.; Li, X.; Lou, F.; Xiong, D.; Ye, L.; Wang, Z. M. Injectable nanocomposite hydrogels with strong antibacterial, osteoinductive, and ROS-scavenging capabilities for periodontitis treatment. *ACS Appl. Mater. Interfaces* **2024**, *16*, 14421–14433.
[16] Deng, D. K.; Li, X.; Zhang, J. J.; Yin, Y.; Tian, Y.; Gan, D.; Wu, R. X.; Wang, J.; Tian, B. M.; Chen, F. M. et al. Biotin-avidin system-based delivery enhances the therapeutic performance of MSC-derived exosomes. *ACS Nano* **2023**, *17*, 8530–8550.
[17] Wang, Y.; Jin, S. S.; Guo, Y. R.; Lu, Y. L.; Deng, X. L. Adhesive and injectable hydrogel microspheres for NRF2-mediated periodontal bone regeneration. *Int. J. Oral Sci.* **2025**, *17*, 7.
[18] Yu, Y. B.; Cheng, Y.; Tong, J. Y.; Zhang, L.; Wei, Y.; Tian, M. Recent advances in thermo-sensitive hydrogels for drug delivery. *J. Mater. Chem. B* **2021**, *9*, 2979–2992.
[19] van Tienen, T. G.; Heijkants, R. G. J. C.; Buma, P.; de Groot, J. H.; Pennings, A. J.; Veth, R. P. H. Tissue ingrowth and degradation of two biodegradable porous polymers with different porosities and pore sizes. *Biomaterials* **2002**, *23*, 1731–1738.
[20] Shi, W. W.; Cassmann, T. J.; Bhagwate, A. V.; Hitosugi, T.; Ip, W. K. E. Lactic acid induces transcriptional repression of macrophage inflammatory response via histone acetylation. *Cell Rep.* **2024**, *43*, 113746.
[21] Chen, S. H.; Xu, Y. N.; Zhuo, W.; Zhang, L. The emerging role of lactate in tumor microenvironment and its clinical relevance. *Cancer Lett.* **2024**, *590*, 216837.
[22] Ma, L.; Li, M.; Komasa, S.; Hontsu, S.; Hashimoto, Y.; Okazaki, J.; Maekawa, K. Effect of Er:YAG Pulsed laser-deposited hydroxyapatite film on titanium implants on M2 macrophage polarization *in vitro* and osteogenesis *in vivo*. *Int. J. Mol. Sci.* **2024**, *25*, 349.
[23] Shang, L. L.; Shao, J. L.; Ge, S. H. Immunomodulatory properties: The accelerant of hydroxyapatite-based materials for bone regeneration. *Tissue Eng. Part C: Methods* **2022**, *28*, 377–392.
[24] Xu, H. Z.; Su, J. S. Restoration of critical defects in the rabbit mandible using osteoblasts and vascular endothelial cells co-cultured with vascular stent-loaded nano-composite scaffolds. *J. Mech. Behav. Biomed. Mater.* **2021**, *124*, 104831.
[25] Wang, D. D.; Wei, L.; Hao, J. L.; Tang, W. F.; Zhou, Y.; Zhang, C. G.; Wang, J. M. PCLLA-nanoHA bone substitute promotes M2 macrophage polarization and improves alveolar bone repair in diabetic environments. *J. Funct. Biomater.* **2023**, *14*, 536.
[26] Yan, C. P.; Zhang, P. R.; Qin, Q. W.; Jiang, K.; Luo, Y.; Xiang, C.; He, J. T.; Chen, L.; Jiang, D. M.; Cui, W. G. et al. 3D-printed bone regeneration scaffolds modulate bone metabolic homeostasis through vascularization for osteoporotic bone defects. *Biomaterials*, **2024**, *311*, 122699.
[27] Deng, J. X.; Yu, W. H.; Zhan, L.; Zhu, X. Y.; Fang, Y. Y.; Zhang, P. C.; Ke, Q. F.; Huang, C. Wettability regulation of membranes based on biodegradable aliphatic polyester. *J. Membr. Sci.* **2024**, *711*, 123199.
[28] Xu, L. C.; Siedlecki, C. A. Effects of surface wettability and contact time on protein adhesion to biomaterial surfaces. *Biomaterials* **2007**, *28*, 3273–3283.
[29] Hao, L. J.; Yang, H.; Du, C.; Fu, X. L.; Zhao, N. R.; Xu, S. J.; Cui, F. Z.; Mao, C. B.; Wang, Y. J. Directing the fate of human and mouse mesenchymal stem cells by hydroxyl-methyl mixed self-assembled monolayers with varying wettability. *J. Mater. Chem. B* **2014**, *2*, 4794–4801.
[30] Wang, H. L.; Boyapati, L. "PASS" principles for predictable bone regeneration. *Implant Dent.* **2006**, *15*, 8–17.
[31] Agrawal, C. M.; Athanasiou, K. A. Technique to control pH in vicinity of biodegrading PLA-PGA implants. *J. Biomed. Mater. Res.* **1997**, *38*, 105–114.
[32] Hajjar, S.; Zhou, X. pH sensing at the intersection of tissue homeostasis and inflammation. *Trends Immunol.* **2023**, *44*, 807–825.
[33] Arce, M.; Endo, N.; Dutzan, N.; Abusleme, L. A reappraisal of microbiome dysbiosis during experimental periodontitis. *Mol. Oral Microbiol.* **2022**, *37*, 180–195.
[34] Ribeiro, A. A.; Jiao, Y. Z.; Girnary, M.; Alves, T.; Chen, L.; Farrell, A.; Wu, D.; Teles, F.; Inohara, N.; Swanson, K. V. et al. Oral biofilm dysbiosis during experimental periodontitis. *Mol. Oral Microbiol.* **2022**, *37*, 256–265.
[35] Ebersole, J. L.; Dawson, D.; Emecen-Huja, P.; Nagarajan, R.; Howard, K.; Grady, M. E.; Thompson, K.; Peyyala, R.; Al-Attar, A.; Lethbridge, K. et al. The periodontal war: Microbes and immunity. *Periodontol. 2000* **2017**, *75*, 52–115.
[36] Basic, A.; Dahlén, G. Microbial metabolites in the pathogenesis of periodontal diseases: A narrative review. *Front. Oral Health* **2023**, *4*, 1210200.
[37] Ross, E. A.; Devitt, A.; Johnson, J. R. Macrophages: The good, the bad, and the gluttony. *Front. Immunol.* **2021**, *12*, 708186.
[38] Xiao, Z. H.; Deng, J. J.; Wei, L.; Zhang, C. N.; Zhong, J. W.; Yang, Y.; Qiao, S. C.; Zhao, J. Bone augmentation of maxillary sinus floor elevation with hydroxyapatite/ poly(lactide-co-caprolactone) composites. *Mater. Today Nano* **2025**, *30*, 100624.
[39] Kazimierczak, P.; Koziol, M.; Przekora, A. The chitosan/agarose/NanoHA bone scaffold-induced M2 macrophage polarization and its effect on osteogenic differentiation *in vitro*. *Int. J. Mol. Sci.* **2021**, *22*, 1109.

[40] Han, N. N.; Liu, Y. T.; Du, J.; Xu, J. J.; Guo, L. J.; Liu, Y. Regulation of the host immune microenvironment in periodontitis and periodontal bone remodeling. *Int. J. Mol. Sci.* **2023**, *24*, 3158.
[41] Liu, H.; Wu, X. L.; Gang, N.; Wang, S. M.; Deng, W.; Zan, L. P.; Yu, S. J. Macrophage functional phenotype can be consecutively and reversibly shifted to adapt to microenvironmental changes. *Int. J. Clin. Exp. Med.* **2015**, *8*, 3044–3053.
[42] Yang, Y. H.; Huang, Y. P.; Li, W. R. Autophagy and its significance in periodontal disease. *J. Periodontal Res.* **2021**, *56*, 18–26.
[43] Liu, L. L.; Guo, H. M.; Song, A. M.; Huang, J. H.; Zhang, Y.; Jin, S. S.; Li, S. T.; Zhang, L. G.; Yang, C. Z.; Yang, P. S. Progranulin inhibits LPS-induced macrophage M1 polarization via NF-κB and MAPK pathways. *BMC Immunol.* **2020**, *21*, 32.
[44] El-Kenawi, A.; Ruffell, B. Inflammation, ROS, and mutagenesis. *Cancer Cell* **2017**, *32*, 727–729.
[45] Chen, L. R.; Zou, Y. M.; Li, R. T.; Zhou, X.; Lai, Y. H.; Chen, J. X.; Yang, J. The hybrid of Cu─TCPP@Mn_3O_4 for inflammation relief by ROS scavenging and O_2 production: An efficient strategy for antiviral therapy. *Small* **2024**, *20*, 2306095.
[46] Lao, A.; Wu, J. Q.; Li, D. J.; Shen, A. L.; Li, Y. X.; Zhuang, Y.; Lin, K. L.; Wu, J. Y.; Liu, J. Q. Functionalized metal-organic framework-modified hydrogel that breaks the vicious cycle of inflammation and ROS for repairing of diabetic bone defects. *Small* **2023**, *19*, 2206919.
[47] Mills, E. L.; Kelly, B.; Logan, A.; Costa, A. S. H.; Varma, M.; Bryant, C. E.; Tourlomousis, P.; Däbritz, J. H. M.; Gottlieb, E.; Latorre, I. et al. Repurposing mitochondria from ATP production to ROS generation drives a pro-inflammatory phenotype in macrophages that depends on succinate oxidation by complex II. *Cell* **2016**, *167*, 457–470.e13.
[48] Du, L. M.; Lin, L. Y.; Li, Q.; Liu, K. L.; Huang, Y.; Wang, X. F.; Cao, K.; Chen, X. D.; Cao, W.; Li, F. Y. et al. IGF-2 preprograms maturing macrophages to acquire oxidative phosphorylation-dependent anti-inflammatory properties. *Cell Metab.* **2019**, *29*, 1363–1375.e8.
[49] Sun, X. D.; Gao, S.; Luo, S. B.; Chang, R. X.; Jia, H. D.; Xu, Q. S.; Jiang, Q. M.; Loor, J. J.; Xu, C. Mitochondrial calcium uniporter regulator 1 (MCUR1) relieves mitochondrial damage induced by lipopolysaccharide by mediating mitochondrial Ca^{2+} homeostasis in bovine mammary epithelial cells. *J. Agric. Food Chem.* **2023**, *71*, 7278–7288.
[50] Wang, X. L.; Sun, R. X.; Li, D. X.; Chen, Z. G.; Li, X. F.; Sun, S. Y.; Lin, F.; Zhao, G. A. Salidroside regulates mitochondrial homeostasis after polarization of RAW264.7 macrophages. *J. Cardiovasc. Pharmacol.* **2023**, *81*, 85–92.
[51] Li, M. Y.; Yang, Y. H.; Xiong, L. T.; Jiang, P.; Wang, J. J.; Li, C. X. Metabolism, metabolites, and macrophages in cancer. *J. Hematol. Oncol.* **2023**, *16*, 80.
[52] Auger, J. P.; Zimmermann, M.; Faas, M.; Stifel, U.; Chambers, D.; Krishnacoumar, B.; Taudte, R. V.; Grund, C.; Erdmann, G.; Scholtysek, C. et al. Metabolic rewiring promotes anti-inflammatory effects of glucocorticoids. *Nature* **2024**, *629*, 184–192.
[53] West, A. P.; Khoury-Hanold, W.; Staron, M.; Tal, M. C.; Pineda, C. M.; Lang, S. M.; Bestwick, M.; Duguay, B. A.; Raimundo, N.; MacDuff, D. A. et al. Mitochondrial DNA stress primes the antiviral innate immune response. *Nature* **2015**, *520*, 553–557.
[54] Zecchini, V.; Paupe, V.; Herranz-Montoya, I.; Janssen, J.; Wortel, I. M. N.; Morris, J. L.; Ferguson, A.; Chowdury, S. R.; Segarra-Mondejar, M.; Costa, A. S. H. et al. Fumarate induces vesicular release of mtDNA to drive innate immunity. *Nature* **2023**, *615*, 499–506.
[55] Zhang, D. Y.; Li, J. Y.; Zhao, L. L.; Yang, Z. H.; Wu, C.; Liu, Y.; Li, W. S.; Jin, Z. D.; Ma, J. Y. Mitochondrial DNA leakage promotes persistent pancreatic acinar cell injury in acute pancreatitis via the cGAS–STING–NF-κB pathway. *Inflammation* **2025**, *48*, 1420–1437.
[56] O'Neill, L. A. J.; Artyomov, M. N. Itaconate: The poster child of metabolic reprogramming in macrophage function. *Nat. Rev. Immunol.* **2019**, *19*, 273–281.
[57] Biswas, S. K.; Mantovani, A. Orchestration of metabolism by macrophages. *Cell Metab.* **2012**, *15*, 432–437.
[58] Kolliniati, O.; Ieronymaki, E.; Vergadi, E.; Tsatsanis, C. Metabolic regulation of macrophage activation. *J. Innate Immun.* **2022**, *14*, 51–68.
[59] Zhou, H. C.; Yan, X. Y.; Yu, W. W.; Liang, X. Q.; Du, X. Y.; Liu, Z. C.; Long, J. P.; Zhao, G. H.; Liu, H. B. Lactic acid in macrophage polarization: The significant role in inflammation and cancer. *Int. Rev. Immunol.* **2022**, *41*, 4–18.
[60] Mahon, O. R.; Browe, D. C.; Gonzalez-Fernandez, T.; Pitacco, P.; Whelan, I. T.; Von Euw, S.; Hobbs, C.; Nicolosi, V.; Cunningham, K. T.; Mills, K. H. G. et al. Nano-particle mediated M2 macrophage polarization enhances bone formation and MSC osteogenesis in an IL-10 dependent manner. *Biomaterials* **2020**, *239*, 119833.
[61] Shanley, L. C.; Mahon, O. R.; O'Rourke, S. A.; Neto, N. G. B.; Monaghan, M. G.; Kelly, D. J.; Dunne, A. Macrophage metabolic profile is altered by hydroxyapatite particle size. *Acta Biomater.* **2023**, *160*, 311–321.
[62] Yoshitomi, T.; Nagasaki, Y. Reactive oxygen species-scavenging nanomedicines for the treatment of oxidative stress injuries. *Adv. Healthc. Mater.* **2014**, *3*, 1149–1161.
[63] Cao, P.; Yu, C. H.; Liu, Y. Q.; Chen, L.; Luan, Q. X.; Liu, J. A modified intrabony defect model of periodontitis in rat. *Oral Dis.* **2025**, *31*, 2261–2272.
[64] Nuerlan, G.; Yu, M.; Wang, X. Y.; Zhang, Y. X.; Li, Y. Y.; Zhang, K. H.; Pan, L.; Ozathaley, A.; Wu, Y. X.; Li, Q. L. et al. Mitochondria replenishment enhances senescent periodontal ligament stem cell osteogenesis and facilitates bone repair. *Nano Res.* **2025**, *18*, 94907375.
[65] Jung, J.; Zeng, H.; Horng, T. Metabolism as a guiding force for immunity. *Nat. Cell Biol.* **2019**, *21*, 85–93.
[66] Zhong, X.; Gong, S. Q.; Meng, L. H.; Yao, W. F.; Du, K.; Jiao, L. C.; Ma, G. W.; Liang, J. W.; Wei, B. B.; Jin, X. et al. Cordycepin modulates microglial M2 polarization coupled with mitochondrial metabolic reprogramming by targeting HKII and PDK2. *Adv. Sci.* **2024**, *11*, 2304687.
[67] Yang, Z. Y.; Xu, J. A.; Kang, T.; Chen, X. P.; Zhou, C. C. The impact of NLRP3 inflammasome on osteoblasts and osteogenic differentiation: A literature review. *J. Inflamm. Res.* **2024**, *17*, 2639–2653.
[68] Hu, Y. Z.; Wang, Z. G.; Fan, C.; Gao, P. Y.; Wang, W. X.; Xie, Y. T.; Xu, Q. C. Human gingival mesenchymal stem cell-derived exosomes cross-regulate the Wnt/β-catenin and NF-κB signalling pathways in the periodontal inflammation microenvironment. *J. Clin. Periodontol.* **2023**, *50*, 796–806.
[69] Wang, D. H.; Zhu, L. L.; Zhang, L. D.; Zhang, G. M.; Qian, Y. P.; Wu, L. Z.; Ma, D. C.; Dai, T. H.; Shan, X. F.; Luo, D. B. et al. Multi-scale composite Ag–TiO_2 nanoreactor for long-lasting antibacterial and immunomodulatory therapy of periodontitis. *Nano Res.* **2025**, *18*, 94907527.
[70] Shen, T.; Dai, K.; Yu, Y. M.; Wang, J.; Liu, C. S. Sulfated chitosan rescues dysfunctional macrophages and accelerates wound healing in diabetic mice. *Acta Biomater.* **2020**, *117*, 192–203.